



IMAGE LICENSED BY INGRAM PUBLISHING

Hybrid Solar-Wind Energy Harvesting for Embedded Applications: Supercapacitor-Based System Architectures and Design Tradeoffs

Mohamadhadi Habibzadeh, Moeen Hassanaliyeragh,
Akihiro Ishikawa, Tolga Soyata, and Gaurav Sharma

Abstract

To enable off-grid deployments of autonomous systems for extended operational durations, robust energy harvesting in the medium power range (1–10 W) is essential. Supercapacitor-based solar energy harvesters have emerged as a popular alternative due to their long lifetime under repeated charge-discharge cycles, low maintenance, environmental friendliness, and energy predictability and scalability. Despite their advantages, such systems are not well matched with applications that require power continuously over their operational lifetime because solar power is unavailable during nights and severely reduced on cloudy days. For such applications, it is beneficial to combine solar power with another power source—such as wind—that exhibits complementary availability. In this paper, we present multiple solar/wind (hybrid) supercapacitor-based harvesters, leveraging existing open-source solar-only harvester designs. Our designs center around three main categories that i) add wind harvesting capability to create a wind-only harvesting system, ii) use multiple harvesters for utilizing hybrid sources of power and for providing fault tolerance, or iii) use a single harvester in a time multiplexed configuration to simultaneously harvest from multiple power sources. We provide extensive experimental results to document the functionality and operational performance of a representative set of these designs.

1. Introduction

Autonomously deployed embedded systems in the medium power (1–10 W) range have recently received broad attention in the literature due to their applications in numerous emerging technologies, including smart cities [1]–[4], environmental monitoring [5], agriculture [6]–[8], and emergency management [9]. These applications typically employ a network of field systems in locations with no or limited power infrastructure, requiring them to incorporate an autonomous ambient power harvesting solution for a seamless operation.

The appropriate energy harvesting approach for an embedded field-deployed system is primarily determined by the power requirements of the target applications. These requirements along with the most commonly harvested ambient power sources are categorized and compared in Table 1 and Table 2, respectively. While embedded systems that operate in the (1 μ W–10 mW) power range can be powered from piezoelectric [21], thermal [22], microbial [23], RF [24], wind [25], and solar [26] energy harvesters, medium-power embedded systems that operate in the (1–10 W) power range rely primarily on solar, wind, or a combination of solar and wind (hybrid) energy harvesters. A rich body of energy harvester designs exists in the literature that accepts solar-only, wind-only, or hybrid solar/wind power inputs and buffer the harvested energy in the rechargeable batteries [27]–[29].

Autonomous solar-only—or wind-only—field systems are susceptible to frequent power interruptions (*downtime*), because neither solar panels nor wind turbines can individually provide continuous power throughout

an entire day. Solutions introduced in the literature alleviate the deficiency of these power sources by buffering the surplus portion of the harvested energy in a large energy buffer such as rechargeable batteries [47], [48] or supercapacitors [49]–[51]. When there is inadequate input power to feed the embedded system (e.g., dark nights or days with no wind), the buffered energy is retrieved to compensate for the shortage. However, if the input power is below the power consumption of the system for an extended period, the buffered energy is eventually depleted, causing a system outage and increasing the downtime [52].

Hybrid harvesters [53]–[57] that can utilize both solar or wind power are attractive because these two sources often have complementary availability. This means that they can meet desired downtime targets without requiring over-provisioning of buffer and panel/turbine resources; an example of this is illustrated in Fig. 1, which depicts the average solar irradiation level and wind speed in the Rochester, NY region over the 2009–2010 calendar years. While the solar power availability peaks between the months of April through August, wind power is the lowest during this period; outside this period, an inverse pattern is observed. In the presence of such complementarity, a hybrid harvester—powered from both solar and wind sources—is expected to provide a much steadier power output as compared to one that has a single power source.

Embedded systems powered by solar/wind harvesting are subject to cyclical and variable availability of power, which implies frequent charge-discharge cycles for the energy buffer used. Supercapacitors are particularly attractive as an energy buffer in these systems because of their much longer lifetime under repeated charging and discharging [58]. The lower energy density

Digital Object Identifier 10.1109/MCAS.2017.2757081

Date of publication: 20 November 2017

M. Habbizadeh and T. Soyata are with the Department of Electrical and Computer Engineering, SUNY Albany, Albany NY, 12203. E-mail: {hhabbizadeh, tsoyata}@albany.edu. M. Hassanaliheragh and G. Sharma are with Department of Electrical and Computer Engineering, University of Rochester, Rochester, NY 14627. E-mail: {mhassanaliheragh, gaurav.sharma}@rochester.edu. A. Ishikawa was with Department of Electrical and Computer Engineering, University of Rochester, Rochester, NY 14627. He is now with Computer Science Department, Carnegie Mellon University, PA, 15213.

Table 1.

Electric devices can be categorized into four distinct groups, based on their power consumption. This table presents the approximate power range of each category because there is no standard definition that clarifies the exact values. Medium power category is the focus of this paper.

Category	Power Range	Comments
Ultra low power	≤ 1 mW	Power consumption typically ranges from multiple pico Watts in standby state to a few milli Watts when fully operational. Applications include smart homes [10], surveillance [11], and environmental monitoring [12]. Authors in [13] develop a sub- μ Watt in-vivo sensing node with energy harvesting capability, which can measure and report the intraocular pressure over a wireless communication link.
Low power	1 mW–1 W	Example applications of low-power devices include smart transportation [14], machine interface [15], and structural health monitoring [16]. Authors in [17] develop a flexible smart sensing node that can be used in various IoT application. Each node has a power consumption of ≈ 100 mW.
Medium power	1 W–10 W	This category comprises embedded systems that have sensors with relatively high power demand (e.g., gas sensors [18] and cameras [19]). Furthermore, devices with relatively complicated pre-processing and feature extraction capabilities, along with many Internet gateways in WSNs, which provide high-rate data transmission and execute complicated routing algorithms fall into this category [20].
High power	≥ 10 W	This category consists of devices that have traditionally been grid-connected with power consumption ranging from multiple Watts for household devices to kilo or mega Watts for industrial systems.

of supercapacitors compared with batteries, however, makes their physical size a critical issue in deployments and this has hindered the adoption of supercapacitors despite their favorable characteristics such as environmental-friendliness, convenient power management, energy predictability, and longer lifetime [59]. Because hybrid harvesting can reduce the required energy buffering capacity, supercapacitors can be immediate beneficiaries of hybrid solar/wind harvesters. In this paper, we propose multiple supercapacitor-based hybrid wind/solar energy harvesters.

Our designs are based on the UR-SolarCap *solar-only* open-source energy harvester [34], which was not originally designed to harvest wind power. As the first step of our design, we introduce the required hardware and software adaptations to convert UR-SolarCap to a *wind-only* harvesting system. As the next step, we propose multiple topologies to implement a *hybrid (wind/solar)* harvesting system using one or more UR-SolarCap boards. Our last step introduces a design variant that harvests multiple power sources using a single UR-SolarCap; for this design, an analog time multiplexing mechanism is introduced that buffers and harvests individual sources in discrete time intervals, thereby reducing the component count substantially to provide a lower-cost harvester alternative.

The rest of the paper is organized as follows. In Sections 2 and 3, we explain the basic characteristics of solar and wind power sources. In Section 4, we analyze the advantages of wind/solar hybrid harvesting using

available measurement data for assessing power availability and models for harvested energy. In Section 5, we describe the general structure of energy harvesting systems. In Section 6, we review the open-source solar-only harvester, UR-SolarCap, and propose modifications to turn it into a wind-only power harvester. The two single-source systems presented in this section are the building-blocks of our hybrid architectures. Section 7 introduces the high-level architectures and characteristics of our hybrid setups. Sections 8 and 9 provide technical details of our implementations. We present the experimental results of the hybrid systems in Section 10.

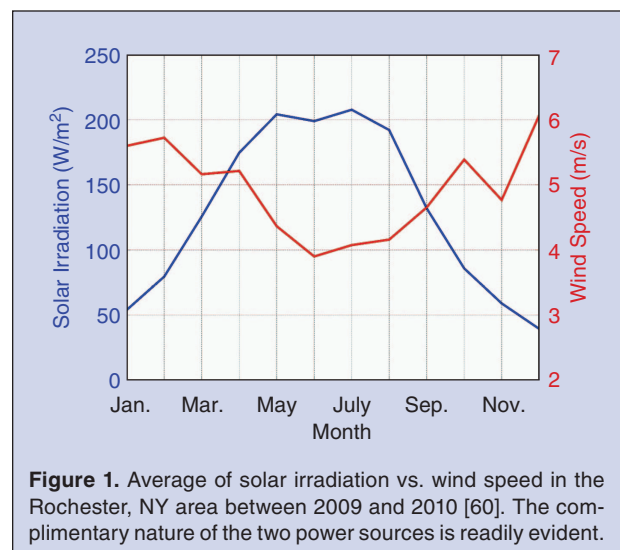


Figure 1. Average of solar irradiation vs. wind speed in the Rochester, NY area between 2009 and 2010 [60]. The complimentary nature of the two power sources is readily evident.

Table 2.

A comparison of power sources for embedded systems. Power reported in decibel milliwatts (P_{dBm}) is computed from the power in milliwatts (P_{mW}) as $P_{dBm} = 10 \log_{10}(P_{mW})$ [30]. Information provided in this table is derived from [31, 32], as well as the sources cited in the *Comments* column of this table. The *Embedded Nominal Power (ENP)* column provides the output power of a typical example of the corresponding power source for an embedded system. Among the listed power sources, only wind and solar can be meaningfully scaled to provide sufficient power for medium-power systems.

Power Source	Type	Typical Power Density	Embedded Nominal Power	Transducer	Comments
Wind	Mechanical	28.5 mW/cm ²	47 dBm (50 W)	Wind Turbine	Power density is dependent on wind speed. The listed power density is measured at a wind speed of 6.3 m/s [33]. 50 W is the ENP of a five-blade (30 cm radius) wind turbine.
Solar	Electromagnetic	15 mW/cm ²	42 dBm (15 W)	Solar Panels (Outdoors) (0–200 KLux)	The listed ENP is reported in [34]. Solar panels can readily be scaled to provide higher or lower power, making them suitable for embedded applications. A 35 × 33 cm ² panel can provide a rated power of 15 W.
Thermal	Thermal	15 μW/cm ³	22 dBm (150 mW)	Thermoelectric Generator (TEG)	The power density is reported for a temperature difference of ΔT = 10°C. Higher densities can be achieved by increasing temperature difference. The ENP is reported in [35] when the hot and cold end temperatures are ≈ 55°C and 21°C, respectively and the TEG size is 30 × 34 × 3.2 mm ³ .
Vibration	Mechanical	145 μW/cm ³	19 dBm (74 mW)	Electromagnetic	Generated power is dependent on the amplitude and frequency of mechanical stimulus and dimensions of the generator [36], [37]. The ENP is reported in [38] for a transducer operating at 54 Hz and acceleration of 0.57 g. The size of the transducer is ≈ 70 cm ³ .
	Mechanical	330 μW/cm ³	-7 dBm (200 μW)	Piezoelectric materials	Power is determined by the type of the piezoelectric material and the intensity of the mechanical strain [39]. The ENP corresponds to the transducer studied in [39], excited with frequency of 120 Hz and the peak applied strain of 200 με. The size of the transducer is 13 × 10 × 0.38 mm ³ .
	Mechanical	50 μW/cm ³	-7 dBm (200 μW)	Electrostatic	Generated power is dependent on the mechanical stimuli and the fabrication process [40]. The ENP is the output power of the system described in [40], at vibration acceleration under 1 g. The transducer is 1 cm ² with a mobile mass of 1 gm.
Microbial	Biochemical	2.6 μW/cm ²	-2 dBm (600 μW)	Microbial Fuel Cell	Power density is dependent on the area of the anode; as it increases, the power density decreases [41]. For smaller anodes, the power density can reach as high as 300 μW/cm ² [42]. The ENP is reported in the same source for a transducer with area of 2 cm ² .
Indoor Lights	Electromagnetic	15 μW/cm ²	-3 dBm (480 μW)	Solar Panels (Indoors) (1 Lux–3 kLux)	Generated power is dependent on the light intensity and ambient temperature. An indoor solar panel is expected to generate orders-of-magnitude lower power, due to its smaller profile and substantially lower solar irradiation. The ENP is reported in [43] at illuminance of around 1 kLux and solar panel area of 65 cm ² .
Directed RF	Electromagnetic	50 mW/cm ²	20 dBm (100 mW)	Antenna	In directed RF power harvesting, a power caster, located in proximity of the power harvester(s) and aimed at certain direction, transmits the RF signal, thereby improving the power density [44]. The ENP is reported in [45], for the transmission power of 910 mW, located 1 m away from the receiver.
Acoustic	Mechanical	96 μW/cm ³	-11 dBm (80 μW)	Microphones/Piezoelectric	Generated power is dependent on the sound pressure level, distance from the source, and the frequency of the sound [46]. The ENP is reported in [46] for a PZT transducer (≈ 1 cm ³) stimulated by a vibration with magnitude of 2.25 m/s ² and frequency of 100 Hz.
Ambient RF	Electromagnetic	12 nW/cm ²	-23 dBm (5 μW)	Antenna	Typical Power Density is highly dependent on the distance from the broadcasting station, type of the antenna, and the frequency band of the wave; the ENP is the average for the 3G (B7x) band in London [24].

We conclude our paper in Section 11 by summarizing the contribution of our paper and suggesting future work.

2. Solar Power Characteristics

Solar is typically the primary power source for autonomous systems, mostly due to three factors:

- (i) Solar power is readily available almost everywhere. Even in enclosed environments, low-irradiation solar power transducers can be employed to generate electricity from available light [61], [62].
- (ii) Solar power transducers provide higher power density compared to other sources; a two to five orders-of-magnitude advantage over RF, thermal, and airflow power sources is reported in [63].
- (iii) Unlike wind turbines and vibration harvesters, solar energy can be harvested through solid-state devices with no moving parts, which translates to higher reliability, longer lifetime, and lower maintenance costs.

Solar power transducers are composed of elementary units called *solar cells* or *photo-diodes* that generate electricity from solar irradiation. The solar cells are connected in series and/or parallel to form a *solar module*, (or alternatively *solar panel*). Table 3 tabulates the notational symbols that are used to quantify the solar power sources.

2.1. Solar Cells (Photo Diodes)

A solar cell is created on a semiconductor substrate, which is a *bandgap* material with a lower energy valence band separated from the conduction band by a forbidden energy gap of about 1 electron volts (eV). Silicon (Si) is the most commonly used semiconductor material with a bandgap (E_G) of approximately 1.1 eV at 273 K. Other semiconductor materials that are used include GaAs [64], Cds/CdTe [65], and Cu(InGa)Se₂ [66].

In the normal pure crystalline state of a semiconductor, electrons completely occupy the valence band and are restricted from acquiring any energy (for instance, kinetic energy of motion necessary to conduct electricity) unless they can cross the bandgap into the (normally) empty conduction band. A photon incident on the semiconductor can excite an electron to transition from the valence band to the conduction band, provided that the photon's energy E_λ exceeds the semiconductor band gap E_G . The energy of a photon is

$$E_\lambda = \frac{hc}{\lambda}, \quad (1)$$

where h denotes the Planck's constant, c is the speed of light in vacuum, and λ is the wavelength of the photon.

Table 3. Notations used to describe solar power sources in Section 2, with equation and section references for each notation.

Notation	Equations	Sections	Description
λ	1	2.1	Wavelength of electromagnetic radiation
E_λ	1	2.1	Energy of a photon at wavelength λ
h, c	1	2.1	Planck's constant; $h = 6.626 \times 10^{-34} \text{ m}^2 \text{ kg/s}$, speed of light in vacuum; $c \approx 3 \times 10^8 \text{ m/s}$
k, T, q	2; 4; 5; 6	2.1; 2.2	Boltzmann's constant; $k = 1.38 \times 10^{-23} \text{ J/K}$, temperature in K, charge of an electron
V_{OC}	2	2.1	Open circuit voltage of a solar cell
I_{SC}	2; 3	2.1; 2.2	Short circuit current of a solar cell, at zero terminal voltage difference
I_0	2; 4; 5; 6	2.1; 2.2	Diode saturation current
I_{ph}	3; 4; 5; 6	2.2	The aggregate current generated by a solar panel when exposed to light
I_{solar}	4	2.2	The output current of a solar panel, which flows through the load
V_{solar}	4; 5	2.2	The output voltage of a solar panel across the terminals of load
α	4; 5; 6	2.2	Diode ideality factor; α is typically between 1 and 2
P_{solar}	5; 7	2.2	The amount of power a solar panel delivers to the load
V_{MPP}	6	2.2	Solar panel output voltage when operating at the Maximum Power Point (MPP)
P_{rated}	7	2.2	Solar power measured at a certain irradiance level
W_{solar}	7	2.2	Instantaneous solar irradiation level (in W/m^2) at a given point in time
W_{rated}	7	2.2	Solar irradiation level (in W/m^2) at which P_{rated} is specified
P_{Solar}^{max}	7	2.2	Maximum power of a harvester imposed by its design and implementation

In a pure semiconductor, the electrons transported to the conduction band by absorption of a photon would quickly transition back into the valence band (emitting a photon in the process). In a solar cell, such recombination is avoided by creating a p-n junction diode. The substrate is *doped* to obtain a *p-type* material by the addition of a small fraction of *acceptor* atoms that have one less electron in their valence shell compared to the semiconductor. The incorporation of these acceptor atoms in the crystal creates empty acceptor energy levels just above the valence band into which electrons can readily transition to conduct electricity. An *n-type* material is similarly obtained by doping the semiconductor with *donor* atoms that have one more electron in their valence shell compared to the semiconductor, which produces occupied donor levels just below the conduction band from which electrons can also readily transition into the conduction band to conduct electricity. A solar cell is obtained by stacking an n-type layer on top of the p-type substrate and adding a metal layer below the p-type semiconductor and a metal grid on top of the n-type layer. Locally, in the vicinity of the p-n junction, the electrons from the donor layers migrate over from the n-type region into the p-type region till an internal electric field is set up that prevents such movement. When the solar cell is exposed to light, this internal electric field quickly moves electrons that transition to the valence band by absorbing a photon across the junction, preventing their recombination. This builds up a voltage difference between the two electrodes formed by the metal layer below the p-type substrate and the metal grid over the n-type layer. Connection of the electrodes to a load causes a current to flow providing electrical power from the solar energy of the photons. A detailed description of solar cell physics can be found in [67].

Short circuit current of a solar cell (I_{SC}) is the current flowing between the two metal layers when they

are short-circuited. The exact value of (I_{SC}) depends on solar irradiation and cell temperature. It is also highly dependent on the physical and chemical characteristics of the p-n junction; it is typically used as a comparison criterion to rate solar cells. Because (I_{SC}) is dependent on the operational condition of the cell, reference short circuit current (I_{SCR}) is typically used to represent the generated current at a specific temperature and solar irradiation level. It is possible to use (I_{SCR}) to calculate (I_{SC}) through either analytic or experimental equations [68]. The performance of a solar cell can also be characterized by measuring its open-circuit voltage (V_{OC}), which represents the voltage difference between the metal layers of p- and n-type layers when they are open-circuited (i.e., measured when the solar cell current is 0 A). V_{OC} can be calculated as:

$$V_{OC} = \frac{kT}{q} \ln\left(\frac{I_{SC}}{I_0} + 1\right), \quad (2)$$

where k is Boltzmann's constant, T is the temperature in Kelvin, q is the absolute value of electron charge, and I_0 represents the diode's saturation current. For a typical solar cell, V_{OC} is around 0.5 V, which is not sufficient in many applications. Higher voltage and current levels can be reached by connecting multiple solar cells in different serial/parallel topologies.

2.2 Solar Panels

Solar panels consist of multiple solar cells connected in a series and/or parallel topology to reach higher output voltages and currents. We will use two terms, *solar panels* and *solar modules*, interchangeably throughout this paper. Despite the internal complexities of solar cells, solar panels can be modeled using the simple circuit shown in Fig. 2, in which the R_1 , R_2 , and R_3 represent the equivalent junction, intrinsic shunt, and intrinsic series resistances of the panel's solar cells, respectively. The diode D_1 represents the equivalent p-n junction of all of the solar cells, which generate a current, I_{ph} , based on the photons that are incident. For example, assuming N parallel-connected solar cells, I_{ph} is:

$$I_{ph} = N \cdot I_{SC}. \quad (3)$$

Assuming a very large R_2 and a relatively small R_3 , the current that flows through the load (I_{solar}) can be estimated as [69]:

$$I_{solar} = I_{ph} - I_0 \left[\exp\left(\frac{q \cdot V_{solar}}{\alpha k T}\right) - 1 \right], \quad (4)$$

where I_0 is the diode saturation current, V_{solar} is the panel's output voltage, α is the diode's ideality factor (typically between 1 and 2), and T is the junction's

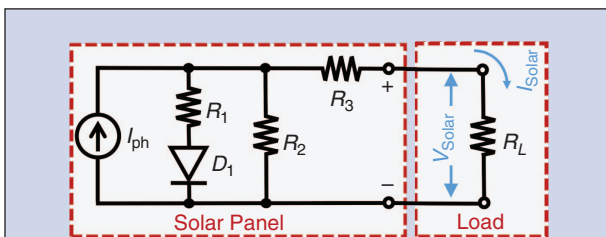


Figure 2. Solar panels can be modeled as a collection of photo cells with an aggregate current of I_{ph} and a diode (D_1) that has a non-linear intrinsic resistance R_1 ; R_2 and R_3 are the equivalent *shunt* and *series* resistances, respectively. The actual values of the circuit elements depend on the characteristics of each solar cell, their quantity, and the topology of their connection [69].

temperature. Using Eq. 4, the generated power of solar panel (P_{solar}) is:

$$P_{\text{solar}} = V_{\text{solar}}(I_{ph} + I_0) - I_0 \cdot V_{\text{solar}} \exp\left(\frac{q \cdot V_{\text{solar}}}{\alpha k T}\right). \quad (5)$$

As can be inferred from Eq. (5), the P-V characteristics of solar panels are non-linear and non-monotonic. For each solar irradiation level, the power reaches a global maximum only at a specific voltage (or equivalently current) value, which is the desirable operating point to extract the maximum amount of power from the solar panel. This optimal operating point is referred to as the Maximum Power Point (MPP) and can be calculated by solving $(dP_{\text{solar}}/dV_{\text{solar}}) = 0$, which yields the equation

$$\frac{I_{ph} + I_0}{I_0} = \left(\frac{q \cdot V_{MPP}}{\alpha k T} + 1\right) \exp\left(\frac{q \cdot V_{MPP}}{\alpha k T}\right), \quad (6)$$

where V_{MPP} is the solar panel output voltage when it is operating at the MPP. Equation (6) indicates that the MPP of a solar panel is a function of I_{ph} and I_0 , which depends on solar irradiation (W_{solar}) and temperature (T). Although Eq. 6 provides a basis for accurate MPP tracking, its implementation in harvesting systems is challenging because of the need to measure solar irradiation, temperature, and the voltage and current of the solar panels. Therefore, several alternative approaches, known as MPP Tracking algorithms (MPPT), have been proposed in the literature, which offer different simplicity vs. accuracy tradeoffs [69]–[75]. The power generated by a solar panel (P_{solar}) at a solar irradiation of W_{solar} is given by the following equation [34]:

$$P_{\text{solar}} = \min\left(P_{\text{rated}} \frac{W_{\text{solar}}}{W_{\text{rated}}}, P_{\text{solar}}^{\text{max}}\right), \quad (7)$$

where the P_{rated} is the rated power output of the solar panel at the rated irradiation level of W_{rated} .

3. Wind Power Characteristics

Wind turbines are used as the primary power source of embedded field devices much less frequently than solar panels because

- (i) The mechanical operation of wind turbines substantially increases system maintenance; even a minor damage to a blade can lead to considerable decrease in generated power, requiring repair or replacement.
- (ii) In contrast with solar power, for which power availability changes are steady and predictable, wind power changes tend to be much more random. The uncertainties about power availability make the system design and provisioning more challenging.
- (iii) Unlike solar panels, wind turbines generate an AC power output, requiring rectification circuitry for

embedded systems that typically operate using DC power.

Despite these limitations, the fact that wind power possesses near-perfect complementary characteristics to solar power (as we detail later in Section 4) makes it an attractive power source for embedded systems that require power availability throughout the day. Table 4 tabulates the notational symbols that are used to quantify the wind power sources.

3.1. Wind Power Source

The kinetic energy E_{wind} of a mass m of air moving with a velocity of v_{wind} can be obtained from standard Newtonian mechanics as

$$E_{\text{wind}} = \frac{1}{2} m v_{\text{wind}}^2. \quad (8)$$

Using Eq. 8, the available power from air flowing through a vertical cylinder with side disc area of A can be calculated as:

$$P_u = \frac{1}{2} \rho \pi R^2 v_{\text{wind}}^3, \quad (9)$$

where v_{wind} is the velocity of the wind arriving at the blades of the turbine, $A = \pi R^2$, and ρ is the air density, which depends on altitude, air temperature, and air chemical composition. When the wind traverses the turbine, kinetic energy from the air gets transferred to the turbine as rotational motion, slowing the wind to a *downstream wind speed* v_{down} that is lower than the *upstream wind speed* v_{wind} . The corresponding wind power decreases from the *upstream wind power* of P_u to the *downstream wind power* P_d obtained by replacing v_{wind} in Eq. 9 with v_{down} . The difference $P_u - P_d$ between the available upstream and downstream wind power is transferred to the turbine, as shown in Fig. 3. The energy transferred to the turbine is typically modeled as [76]:

$$P_{\text{wind}} = \frac{1}{2} C_p(\Lambda, \beta) \rho \pi R^2 v_{\text{wind}}^3, \quad (10)$$

where C_p is the turbine power coefficient, which is based on the turbine's pitch angle (β) and the ratio Λ of its blades' circumferential speed to the velocity of upstream wind flow. For each value of upstream wind speed v_{wind} , Eq. 10 determines an optimal value Λ_{opt} for Λ that achieves the maximum power output P_{max} . To use Eq. 10 in that Maximum Power Point Tracking (MPPT) algorithms additional sensors for measuring the turbine's rotational speed and upstream wind speed are required. Several MPPT approaches are introduced in the literature that use speed sensors or rely on use of adaptive algorithms to eliminate the need for sensors [76]–[80].

Table 4.**Notation used to describe wind power sources in Section 3, with equation and section references for each notation.**

Notation	Equations	Sections	Description
E_{wind}	8	3.1	Kinetic energy of a mass of air particles flowing with the speed of v_{wind}
m	8	3.1	Mass (of a volume of air)
P_u	9	3.1	Kinetic power of a mass of air flowing into a wind turbine (upstream)
v_{wind}	8–10; 12; 13; 15–18	3.1; 3.3; 3.4	Speed of upstream wind, arriving at the blades. $v_{wind} = v_u$
P_{wind}	9; 10	3.1	Power captured by a wind turbine, a portion of P_u
ρ	9; 10	3.1	Air mass density
R	9; 10	3.1	Radius of circle spanned by the rotating turbine blades
$C_p(\Lambda, \beta)$	10	3.1	Wind turbine power coefficient
Λ	10	3.1	Ratio of blade circumferential speed (at the tip) to velocity of upstream wind flow
Λ_{opt}	10	3.1	Optimal ratio of blade circumferential speed (at the tip) to velocity of upstream wind flow
β	10	3.1	Turbine's pitch angle
V_s	13; 14; 15	3.3	Wind turbine stator voltage
K	13; 15	3.3	A constant representing physical properties of a wind turbine
ϕ	13; 14; 15	3.3	Electromagnetic flux of the permanent magnet (in the stator)
ω	12; 13	3.3	Angular velocity of a wind turbine's blades
$V_{turbine}$	14	3.3	Wind turbine output voltage
$P_{turbine}$	14; 15; 16; 17	3.3; 3.4	Wind turbine output power
X_s	14; 15	3.3	Wind turbine synchronous reactance
R_A	14; 15	3.3	Wind turbine stator winding resistance
D	11; 12; 13; 14; 15; 16	3.3	Harvester duty cycle to emulate a variable load
$R_L(D)$	11; 12; 14	3.3	Wind turbine equivalent load as a function of duty cycle
R_{cons}	11	3.3	Wind turbine load
$K_{turbine}$	16	3.3	A wind turbine-specific constant to describe the wind MPP
D_{opt}	16	3.3	Duty cycle at which maximum amount of power is extracted
$v_{cut-out}$	17	3.4	Wind turbine cut-out speed
v_{cut-in}	17	3.4	Wind turbine cut-in speed
v_{rated}	17	3.4	Wind speed at which the turbine delivers a power of P_{rated}
P_{rated}	17	3.4	Rated power output of a wind turbine @ v_{rated}
$f(v_{wind})$	17; 18	3.4	Generated power of wind turbine expressed as a function of wind speed
$C1, C2, C3$	18	3.4	Characteristic parameters of a wind generator determined by cut-in and cut-out speeds

3.2. Wind Turbine Types

For the conversion of mechanical power into electric power, wind turbines used in embedded systems typically employ a variable speed induction generator. A representative design for such a system is shown in Fig. 3. Wind turbine generators (WTGs) are constructed using two parts, a *rotor* and a *stator*, and operate based on the principles of elec-

tromagnetic induction. A turbine's blades capture the mechanical power of the air flow and transfer it to the *rotor*; the rotational movement of the rotor generates a changing electromagnetic field, which induces a voltage difference across the windings of the *stator*.

In synchronous turbines used for grid applications, the electromagnetic field within the generator is created

by the rotor's *field circuit*, which acts as a magnet and creates an electromagnetic field when a DC current is applied to it. Alternatively, the rotor can be constructed from permanent magnets, thereby eliminating the need to continuously supply a DC current. Induction generators maintain their electromagnetic field by drawing reactive power from the grid. For off-grid applications, a block of capacitors is added to the generator to provide reactive power. This technique is referred to as *self-excitation*. Although induction generators are relatively more reliable and less expensive, permanent-magnet synchronous generators are usually used in off-grid medium-power wind turbines due to their ability to drive reactive loads and their independence from grid and self-excitation capacitors.

Similar to electric generators, wind turbines generate three-phase AC power. Because typical embedded systems require a constant DC voltage input, the output of the turbine must be rectified. A detailed explanation of synchronous and induction generators can be found in [81].

3.3. Permanent-Magnet WTG Equivalent Circuit

In this section, we focus our discussion on permanent magnet Wind Turbine Generators (WTGs) (which are also representative of the WTG used in our experiments in Section 10). Because permanent-magnet synchronous generators do not include a field circuit, their output voltage cannot be controlled by manipulating their field circuit current. A voltage regulator is therefore required to produce a constant DC output from the rectified voltage.

Switching regulators are typically preferred due to their high efficiency and their ability to boost and/or reduce the voltage. Once rectified and regulated, the output power can be used to drive a load. From the wind turbine's perspective, the voltage rectifier, switching voltage regulator, and the load appear as a single equivalent load resistance (R_L), which is controlled by the switching duty cycle (D) of the switching voltage regulator [82]. We can show that for a switching regulator such as Single-Ended Primary Inductor Converter (SEPIC) and a rectifier bridge, $R_L(D)$ can be represented as [82]:

$$R_L(D) = \frac{\pi^2}{18} \cdot (1 - D) \cdot R_{\text{cons}} = f_1(D), \quad (11)$$

where R_{cons} is the actual load resistor and is assumed to be constant. The rotational speed (ω) of the WTG is dependent on the load resistance, as well as the wind speed, written as:

$$\omega = f(R_L, v_{\text{wind}}) = f_2(D, v_{\text{wind}}). \quad (12)$$

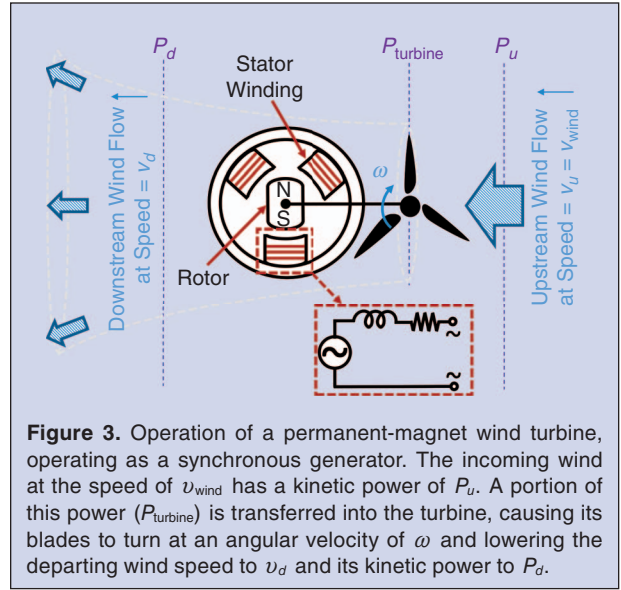


Figure 3. Operation of a permanent-magnet wind turbine, operating as a synchronous generator. The incoming wind at the speed of v_{wind} has a kinetic power of P_u . A portion of this power (P_{turbine}) is transferred into the turbine, causing its blades to turn at an angular velocity of ω and lowering the departing wind speed to v_d and its kinetic power to P_d .

Figure 4 depicts the equivalent per phase circuit of a generic permanent-magnet synchronous generator. V_s represents the magnitude of electromagnetic force induced in the stator that depends on the rotational speed as:

$$V_s = K \cdot \phi \cdot \omega = K \cdot \phi \cdot f_2(D, v_{\text{wind}}), \quad (13)$$

where ϕ is the electromagnetic flux, which is determined by the characteristics of the permanent magnet in the WTG. X_s represents the magnitude of generator synchronous reactance and R_A is the winding resistance. The power output of the WTG is then obtained as

$$V_{\text{turbine}} = V_s \cdot \frac{R_L}{R_L + jX_s + R_A}, \quad (14)$$

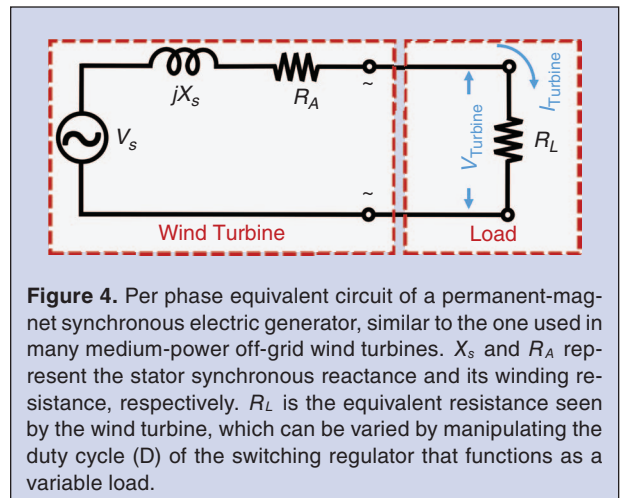


Figure 4. Per phase equivalent circuit of a permanent-magnet synchronous electric generator, similar to the one used in many medium-power off-grid wind turbines. X_s and R_A represent the stator synchronous reactance and its winding resistance, respectively. R_L is the equivalent resistance seen by the wind turbine, which can be varied by manipulating the duty cycle (D) of the switching regulator that functions as a variable load.

$$\begin{aligned}
P_{\text{turbine}} &= \frac{V_{\text{turbine}}^2}{R_L} = V_s^2 \cdot \frac{R_L}{(R_L + jX_s + R_A)^2} \\
&= V_s^2 \cdot f_3(D) \\
&= K^2 \cdot \phi^2 \cdot f_3(D) \cdot f_2^2(D, v_{\text{wind}}).
\end{aligned} \tag{15}$$

Although, one cannot usually obtain a closed-form solution, Eq. 15 implies that the output power of the wind turbine is dependent on turbine implementation, wind speed (through rotor angular velocity ω), and the equivalent variable load $R_L(D)$. Conceptually, the optimum duty cycle (D_{opt}) that generates the maximum output power can be obtained using calculus of variations:

$$\frac{dP_{\text{turbine}}}{dD} = 0 \Rightarrow D_{\text{opt}} = K_{\text{turbine}} \cdot f_{\text{turbine}}(v_{\text{wind}}), \tag{16}$$

where K_{turbine} is a turbine-specific constant, v is the wind speed, and f_{turbine} is a function that is determined by the load curve of the wind turbine. In accordance with Eq. 16, the extracted power from the wind turbine can be manipulated by adjusting the duty cycle of the load based on the wind speed (i.e., the availability of the wind power), assuming that the load is being emulated by a switch mode circuit such as SEPIC [34], [50].

3.4. Wind Turbine Power Limitations

The amount of power a wind turbine can generate is further limited by its design and manufacturing properties. Typically, the turbine's generated power (P_{turbine}) is represented as a function of the wind speed v_{wind} as

$$P_{\text{turbine}} = \begin{cases} 0 & v_{\text{wind}} \leq v_{\text{cut-in}}, \\ f(v_{\text{wind}}) & v_{\text{cut-in}} < v_{\text{wind}} < v_{\text{rated}}, \\ P_{\text{rated}} & v_{\text{rated}} \leq v_{\text{wind}} < v_{\text{cut-out}}, \\ 0 & v_{\text{wind}} \geq v_{\text{cut-out}}, \end{cases} \tag{17}$$

where $v_{\text{cut-in}}$, v_{rated} , and $v_{\text{cut-out}}$ represent, respectively, the cut-in, rated and cut-out speeds. When the wind

speed is below $v_{\text{cut-in}}$, the blades of the generator do not turn and no power is generated. For wind speeds in the range $v_{\text{cut-in}} < v_{\text{wind}} < v_{\text{rated}}$, the generated power varies with the wind speed ($f(v_{\text{wind}})$). The speed v_{rated} in Eq. 17 represents the wind speed at which the turbine reaches its highest generated power (P_{rated}) and this speed is determined by design restrictions. For wind speeds in the range $v_{\text{rated}} \leq v_{\text{wind}} < v_{\text{cut-out}}$, the output power remains at P_{rated} . Under extreme condition where $v_{\text{wind}} \geq v_{\text{cut-out}}$ the wind turbine shuts down to prevent a mechanical damage and the power is reduced to zero. Regressions models are typically used to quantify $f(v_{\text{wind}})$, for instance, as a second order polynomial [84] or cubic power curve [85]. A typical second order polynomial formulation is:

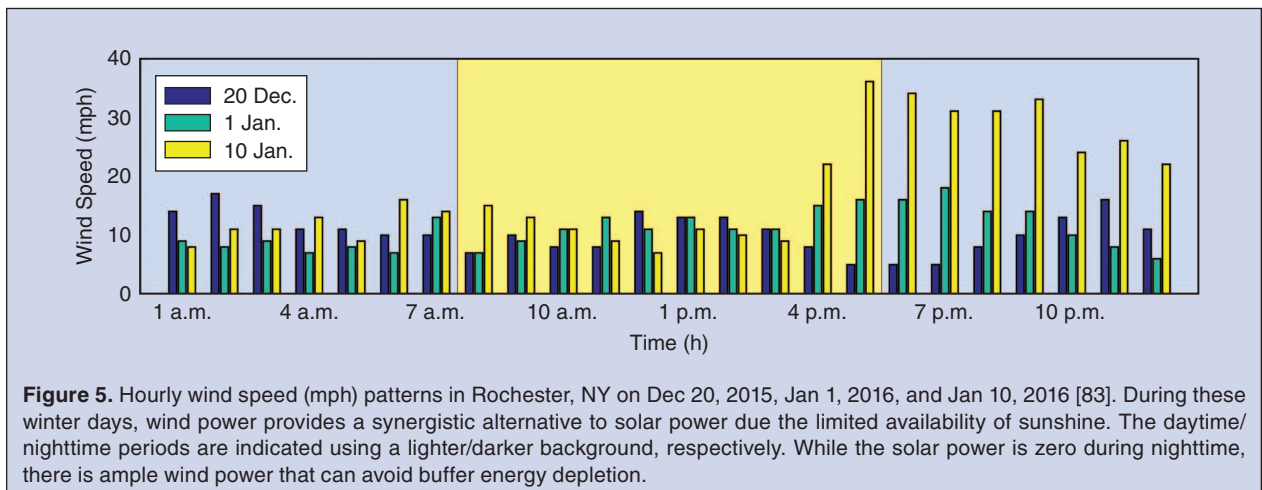
$$f(v_{\text{wind}}) = C_1 + C_2 v_{\text{wind}} + C_3 v_{\text{wind}}^2, \tag{18}$$

where C_1, C_2 , and C_3 are the characteristic parameters of the wind generator.

4. Hybrid Energy Harvesting

Although Fig. 1 demonstrates a near-perfect complementary nature of solar and wind power sources over a full year window, the figure lacks critical detail about the daily availability patterns of these two power sources. An analysis of the complementary nature of solar/wind power sources is necessary at a *daily* rather than *annual* scale because in most embedded systems the daily variation is the main consideration in allocating the size of the energy buffer (supercapacitors in our experimental setup).

Figure 5 demonstrates the hourly instantaneous wind speed in the Rochester, NY area over three randomly-selected days of Fall 2015 and Winter 2016. We selected winter days when the average generated power of solar



panels is relatively low compared to summer days and the system can significantly benefit from hybrid energy harvesting, thereby making the analysis conservative. The areas with blue background in Fig. 5 represent the nighttime (midnight – 8 AM), during which solar panels do not generate any power; however, ample wind power is available on all three days, especially on December 20, 2015. Although the hour-by-hour characteristics of the wind power are stochastic, we are primarily interested in determining the cumulative power available during the nighttime because a typical supercapacitor block can buffer the harvested energy, largely eliminating impact of hourly fluctuations.

4.1. Quantifying The Complementary Characteristics of Solar and Wind Power Sources

To highlight and quantify the advantages of hybrid solar/wind energy harvesting, we use the metric of average downtime, $t_{\text{down}}^{\text{yr}}$, defined as the average number of hours per year for which the system shuts down due to lack of power. The average downtime can be modeled using historically recorded data of solar irradiation and wind speed at the deployment location. Solar irradiation [60] and wind speed [83] data of US cities are available as an average value over $\Delta t = 1$ hour intervals. To calculate $t_{\text{down}}^{\text{yr}}$, we assume that the system is simultaneously harvesting energy from a solar panel and a wind turbine with the rated powers of $P_{\text{solar}}^{\text{rated}}$ and $P_{\text{wind}}^{\text{rated}}$, respectively. The energy is buffered in a supercapacitor block with the maximum energy storage capacity of $E_{\text{SC}}^{\text{max}}$ and it is delivered to a load demanding P_{load} Watts of power. Although the analysis is generally for a hybrid case, it can be easily adapted for a single source scenario by setting $P_{\text{wind}}^{\text{rated}}$ or $P_{\text{solar}}^{\text{rated}}$ to zero. Table 5 tabulates the notations used in this section to quantify hybrid power sources.

In this analysis, our goal is to determine the available energy in a system on an hour-by-hour basis through the 24 hours of a day; for this, we use the notation $P_{\text{in}}(n)$ to denote the average available power during the n th hour of the day. This power is related to the solar ($P_{\text{solar}}(n)$) and wind power ($P_{\text{wind}}(n)$) generation as:

$$P_{\text{in}}(n) = P_{\text{solar}}(n) + P_{\text{wind}}(n). \quad (19)$$

We use the solar irradiation data available in [60] to compute the available average solar power during the n th hour of the day ($P_{\text{solar}}(n)$). We refer to Eq. 7 and assume a specific solar panel size to arrive at $P_{\text{solar}}(n)$. Similarly, we use the wind speed data from [83] and apply it to Eq. 17 to determine the wind power during the n th hour of the day ($P_{\text{wind}}(n)$) by making a similar assumption on the size of the wind turbine.

Table 5. Notation used to describe hybrid power sources in Section 4, along with equation numbers they appear in.

Notation	Equations	Description
$P_{\text{in}}(n)$	19; 20; 22	Average total power during n th interval
$P_{\text{solar}}(n)$	19	Average P_{solar} during n th interval
$P_{\text{wind}}(n)$	19	Average P_{wind} during n th interval
$E_{\text{SC}}^{\text{max}}$	21	Max. energy capacity of supercap. block
$E_{\text{Acc}}(n)$	21; 20; 22	Accumulated energy up to n th interval
$E(n)$	21; 20; 22	Stored energy at end of n th interval
P_{load}	20; 22	Power consumed by load
$\Delta t_{\text{down}}(n)$	22; 23	Downtime contribution of n th interval
P_{load}	22; 20	Power consumption of the load
$t_{\text{down}}^{\text{yr}}$	23	Annual downtime

During the n th time interval, an average power of $P_{\text{in}}(n)$ is generated from both solar and wind power sources (Eq. 19). We assume that the power consumption of the load (P_{load}) is constant throughout the entire simulation period (alternative load profiles are readily incorporated). Therefore, based on whether the load consumption is higher than the generated power or not, a shortage ($P_{\text{in}} < P_{\text{load}}$) or a surplus ($P_{\text{in}} > P_{\text{load}}$) in the energy occurs, which in turn depletes or charges the supercapacitor block, respectively. We use the notation $E(n)$ to refer to the stored and available energy in the supercapacitor block at the end of the n th interval. Furthermore, the notation $E_{\text{Acc}}(n)$ denotes the accumulated energy up to the n th time interval. The relationship between $E(n)$ and $E_{\text{Acc}}(n)$ can be formulated via the recursions:

$$E_{\text{Acc}}(n) = E(n-1) + \Delta t \cdot (P_{\text{in}}(n) - P_{\text{load}}), \quad (20)$$

$$E(n) = \min[\max(E_{\text{Acc}}(n), 0), E_{\text{SC}}^{\text{max}}], \quad (21)$$

where $E_{\text{SC}}^{\text{max}}$ is the energy storage capacity of the supercapacitor block, which cannot be enforced by the harvester through an over voltage limitation mechanism [34]. In Eq. 20, Δt denotes the duration of the time interval (1 hour), $P_{\text{in}}(n) - P_{\text{load}}$ denotes the power surplus or shortage; therefore, their product ($\Delta t \cdot (P_{\text{in}}(n) - P_{\text{load}})$) is the accumulated energy during the n th time interval. Equation 20 implies that a device that is powered from a

supercapacitor block will be down if $E_{\text{Acc}}(n) < 0$ for any time interval n . Because the end goal of our simulation is to calculate the cumulative downtime throughout the entire year, we define $\Delta t_{\text{down}}(n)$ as the contribution to downtime due to time interval n , as follows:

$$\Delta t_{\text{down}}(n) = \begin{cases} 0 & E_{\text{Acc}}(n) \geq 0, \\ \Delta t - \frac{E(n-1)}{P_{\text{load}} - P_{\text{in}}(n)} & E_{\text{Acc}}(n) < 0. \end{cases} \quad (22)$$

Equation 22 implies that if the accumulated energy at the end of the n th interval is positive, there is no contribution to downtime, whereas, a negative accumulated energy implies a downtime of $\Delta t - E(n-1)/(P_{\text{load}} - P_{\text{in}}(n))$, which is added to the down counter ($\Delta t_{\text{down}}(n)$). To compute the downtime throughout the entire year, the contributions of every period throughout the year must be summed to obtain

$$t_{\text{down}}^{\text{yr}} = \left(\frac{\sum_n \Delta t_{\text{down}}(n)}{\sum_n \Delta t} \right) \times 365 \times 24. \quad (23)$$

4.2. A Visual Tool for Solar Panel and Wind Turbine Provisioning

To allow system designers to provision a supercapacitor block and a solar panel based on the needs of their applications, we present a visualization-based tool for downtime analysis. As an example, $t_{\text{down}}^{\text{yr}}$ is plotted in Fig. 6 for a system with a load demand of $P_{\text{load}} = 2$ W; this plot allows system designers to choose a wind turbine size (x -axis) with the rated power in Watts and a supercapacitor block size (y -axis) with a maximum energy storage capacity in terms of Watt hours (Wh). The average downtime is estimated for single source (Fig. 6(a) and Fig. 6(c)) and hybrid configurations (Fig. 6(b) and Fig. 6(d)).

As a demonstration of our visual tool in Fig. 6, we want to calculate the total downtime in a year for an embedded system that consumes a constant 2 W to operate, under different power source scenarios:

- **Solar only (Fig. 6(a)):** If we assume a 60 W solar panel ($P_{\text{solar}}^{\text{rated}} = 60$ W) and a supercapacitor block of $E_{\text{SC}}^{\text{max}} = 25$ Wh, the intersection of the x -axis and y -axis lands in the contours between 320 and 640 hours. Therefore, our estimated downtime is ≈ 480 hours for the entire year (20 days out of 365). Because 25 Wh equals 90000 Joules, this supercapacitor block would require approximately 8 Maxwell 3000 F individual supercapacitors [50]. To reduce the downtime, a larger supercapacitor block can be used; for example, increasing the supercapacitor block size to 30 Wh (108 kJ) reduces the downtime to approximately 160 hours

(≈ 7 days), requiring 10 Maxwell 3000 F supercapacitors. Alternatively, the same downtime can be achieved by using the same supercapacitor block and a larger solar panel with $P_{\text{solar}}^{\text{rated}} = 90$ W.

- **Wind only (Fig. 6(c)):** To keep the downtime at approximately 600 hours (25 days) within a year for an embedded system that has the same supercapacitor block ($E_{\text{SC}}^{\text{max}} = 25$ Wh), we observe that a wind turbine with the rated power of $P_{\text{wind}}^{\text{rated}} = 100$ W is needed.
- **Hybrid ($P_{\text{wind}}^{\text{rated}} = 30$ W) (Fig. 6(b)):** In this scenario, we assume a 30 W wind turbine and use a $P_{\text{solar}}^{\text{rated}} = 30$ W solar panel. Our goal is to reduce the required supercapacitor block size to achieve the same 480 h downtime, computed in the solar only case, where we use a single $P_{\text{solar}}^{\text{rated}} = 60$ W solar panel. Figure 6(b) indicates that a 12 Wh supercapacitor block is required to achieve this goal, translating to four Maxwell 3000 F supercapacitors. Therefore, we conclude that the usage of the hybrid sources (30W + 30W) rather than solar-only (60W) allows us to reduce the required supercapacitor block size to half, owing to the complementary nature of the hybrid sources.
- **Hybrid ($P_{\text{solar}}^{\text{rated}} = 30$ W) (Fig. 6(d)):** In this scenario, we keep the supercapacitor block the same and use solar and wind sources with the same 30 W power rating. We observe from Fig. 6(d) that our downtime reduces to ≈ 40 hours (≤ 2 days) in a year. Therefore, we conclude that using complementary hybrid power sources without a reduction in supercapacitor size provides a drastically reduced downtime.

5. Energy Harvesting Systems

Almost all energy harvesting systems leverage the same architecture, shown in Fig. 7. We first investigate this architecture in Section 5.1 and then discuss how various hybrid harvesters can be implemented atop of this architecture in Section 5.2.

5.1. Harvesting Architecture

The general architecture of a conventional energy harvester is depicted in Fig. 7, which consists of four components: (i) power sources, (ii) pre-conditioner, (iii) harvester, and (iv) energy buffer. Some of these components may not exist in a set of harvesters; for example, *pre-conditioning* is not necessary for most of the solar harvesters. We now examine the details of each component.

Power sources: this component comprises the harvestable source and a transducer to convert it to electrical power. Our proposed systems in this paper include

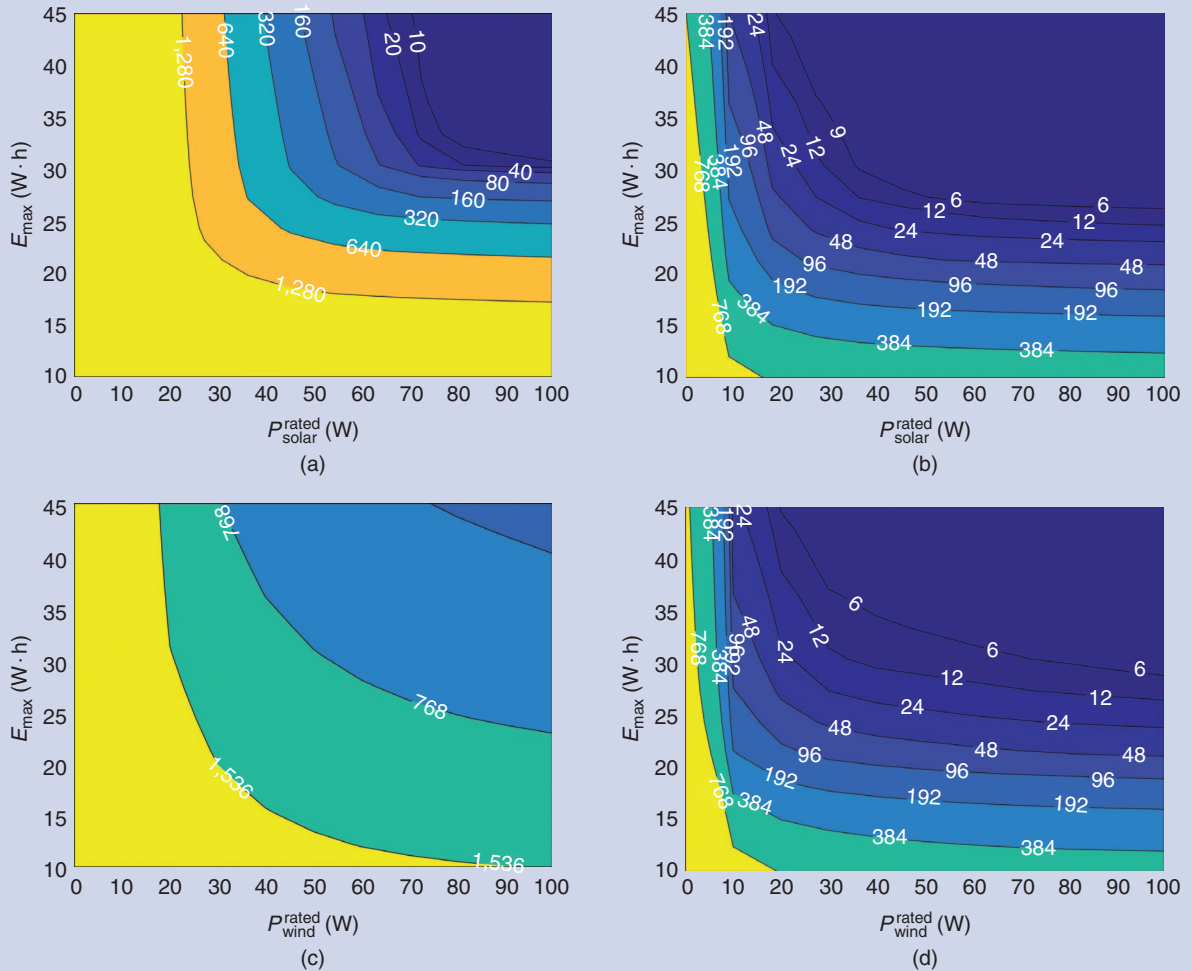


Figure 6. Average downtime ($t_{\text{down}}^{\text{yr}}$) contours in hours/year for a system requiring a P_{load} of 2 W for single source (Fig. 6(a) and Fig. 6(c)) and hybrid configuration (Fig. 6(b) and Fig. 6(d)). The average downtime is estimated for a location in Rochester, NY region based on the recorded solar irradiation and wind speed data during the years 2009–2010 [60], [83]. In single source scenarios, $t_{\text{down}}^{\text{yr}}$ decreases as the size of the power source (P_{rated}) and maximum energy storage ($E_{\text{SC}}^{\text{max}}$) increase. However, adding a second source (wind or solar) with a reasonable size, reduces $t_{\text{down}}^{\text{yr}}$ by an order of magnitude without the need to significantly increase the energy buffer size. (a) Single source solar harvesting ($P_{\text{solar}}^{\text{rated}} = 0$ W). (b) Hybrid harvesting with $P_{\text{solar}}^{\text{rated}} = 30$ W. (c) Single source wind harvesting ($P_{\text{solar}}^{\text{rated}} = 0$ W) and (d) Hybrid harvesting with $P_{\text{solar}}^{\text{rated}} = 30$ W.

solar panels and wind turbines as power sources. A multitude of other power sources and transducers are investigated in the literature [44], [86], [87]. Throughout the rest of this paper, we will use the term *single-source* to refer to solar-only or wind-only; alternatively, we use *multi-source* to refer to systems with more than one power source. Note that solar/solar is considered a hybrid source, because, for example, two solar panels oriented at different angles can provide power in a complementary manner.

Pre-conditioner: pre-conditioning serves three main purposes: **(i)** a voltage rectifier turns the AC power inputs to DC, which is what the *harvesting* component requires; this is necessary for power sources that generate

an AC electrical power, such as a wind turbine as shown in Section 3, **(ii)** a multiplexer allows the selection of one of the power inputs, **(iii)** a voltage limiter component prevents the *harvesting* component from being damaged due to over-voltage. For μ -power harvesters [30] that generate voltages in the mV range, a voltage limiter is generally not necessary, for example, to power the IoT devices (e.g., Wireless Body Area Networks) found in Medical Cyber Physical Systems [88]–[90]. However, for the wind (and some solar) power sources described in this paper, the generated voltage can exceed 100 V requiring a *Pre-conditioning* component to incorporate the power sources in typical harvester circuits that use 25–30 V MOSFETs and diodes.

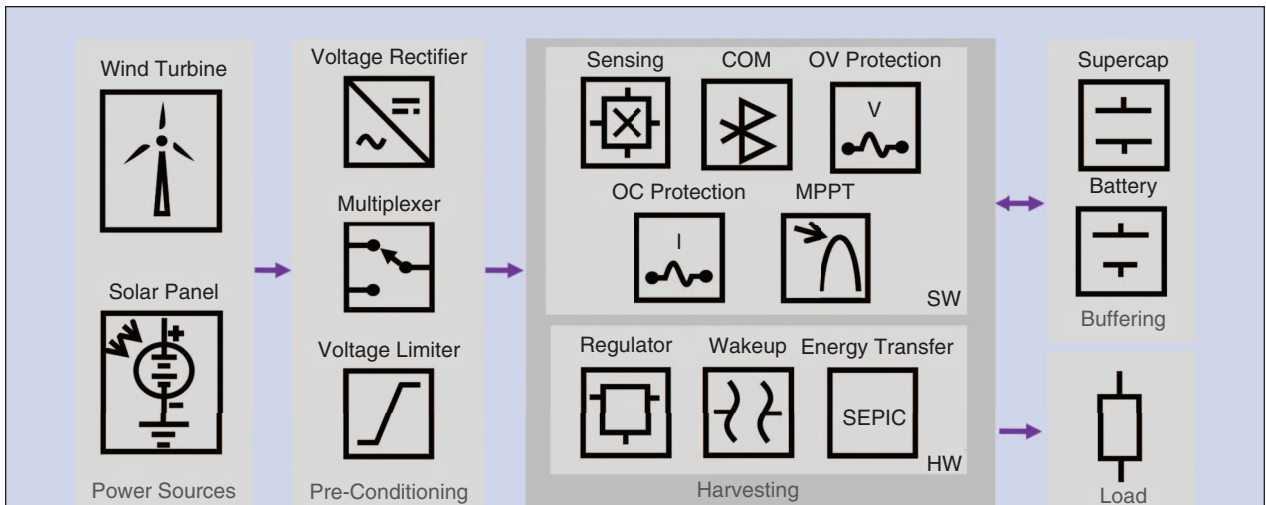


Figure 7. A typical energy harvesting system is composed of five components: (i) *Power Sources* include transducers that output the harnessed power as electrical power; (ii) *Pre-conditioner* performs necessary rectification and over-voltage limiting; (iii) *Harvester* contains the energy harvesting hardware (HW) and firmware to execute harvesting algorithms and provide features such as over-voltage (OV) and over-current (OC) protection; (iv) *Energy Buffer* buffers the harvested energy using batteries or supercapacitors. (v) *Load* represents a sensing node or an actuator, with processing and communication capabilities.

Harvester: this component is responsible for turning the input power into buffered energy (i.e., harvesting). Although the harvester can be implemented using basic hardware elements that do not require software to operate (e.g., OPAMPs, comparators, RLC), for greater efficiency, intelligent configurations are typically controlled by firmware running on a microcontroller or a DSP. The harvesting component incorporates not only the energy harvesting hardware (e.g., inductors, capacitors, switching MOSFETs), but also the firmware to execute the algorithms, such as the MPPT algorithm introduced in Section 2.2; having software-based intelligent harvesters, including the very one we introduce in this paper, provides additional functionality such as over-voltage protection, voltage regulation, and Bluetooth communication with the embedded device that is being powered.

Energy buffer: buffering the harvested energy is crucial to system’s sustainability, as discussed in Section 1. A plethora of energy buffering solutions are studied in the literature [54]; batteries and supercapacitors are commonly used, either individually or in combination. One of the responsibilities of the firmware in the harvester is to implement over-voltage protection for the energy buffer; for example, a series connection of 8 Maxwell 3000 F supercapacitors is employed in [50], which has a voltage limit of $\approx 20\text{--}22$ V, where the variability is determined based on the manufacturing tolerances of the supercapacitors. Therefore, a software-set over-voltage limit must be imposed in the harvester to

prevent damage to the supercapacitors, which, in some situations, may also be potentially hazardous. Note that this is analogous to the over-voltage limits that must be imposed for rechargeable batteries [91].

Embedded System: the harvested energy is ultimately used to power an autonomously operating embedded system. Examples of such systems include medium-power sensors such as cameras for embedded and distributed computer vision applications. Additionally, lower power sensors can be paired with on-node processing devices such as Digital Signal Processors (DSPs), microcontrollers, and tablets to provide on-site feature extraction [92] and noise reduction capabilities [93], which are often used to overcome data transfer limitations. Additionally, network gateways that are used in low-power WSNs often consume orders of magnitude more power than individual nodes, and these may form the load powered by a medium-power harvester.

5.2. Taxonomy for Energy Harvesting Systems

A large family of harvesting systems that we detail in the following sections are capable of harvesting energy from one or more power sources. To categorize these systems in a concise manner, we introduce a taxonomy that distinguishes each harvesting system based on their power sources. Systems that solely depend on a solar power input are denoted using an S symbol, which means *solar-only power input*. Similarly, we use W to refer to wind energy harvesting systems that depend on a *wind-only power input*. To extend this notation to include

systems with more than one power input, we use the notations *SW* (*solar and wind*), *SS* (*double solar*), and *WW* (*double wind*), which imply two power sources, and *SSW* (*double solar and wind*), *SWW* (*solar and double wind*), and *SSS* (*triple solar*), which imply three power sources.

In a practical implementation, *WW* represents a harvesting system that includes two independent wind turbines. Although a single larger wind turbine can also be used in a *W* configuration, having two wind turbines that are physically placed at two locations with different daily/hourly wind patterns can allow each turbine to supply a power input with complementary characteristics; therefore, although each individual power source is of the same type, their combination can be thought as being a hybrid power source. Similarly, the *WWW* configuration can allow a power input from three complementary wind power sources. Furthermore, the *WW* and *WWW* categories can be used to incorporate a fault tolerance advantage into the system, when compared to *W* configuration; for example, if one of the wind turbines breaks and stops providing a power input in a *WWW* configuration, the other wind turbines can still be used to generate some power, as a *WW*. The *SS* and *SSS* configurations can be used to gain similar advantages; solar panels placed at different angles can provide complementary solar power, while using multiple power panels can also make the system fault tolerant against solar panels failures. The *SSW* and *SWW* configurations can further improve the fault tolerance and hybrid input advantages; for example, the *SSW* configuration not only allows for two solar panels placed at different angles but also takes advantage of sources with inherently complementary characteristics.

We introduce the open source UR-SolarCap [34] solar-only (*S*) harvester in Section 6 and the hardware/firmware modifications to operate as a wind only (*W*) harvester. In Section 7 and Section 8, we will introduce designs to allow not only multiple power sources (*multi-source*) but also harvesting systems that use multiple UR-SolarCap boards (*multi-board*). In Section 9, we will introduce the multi-source single-board design variant.

6. Single-Source Harvesting Systems

All of the designs that we present throughout the rest of this paper use the UR-SolarCap system [34] as their building block; UR-SolarCap is an open source solar-only (*S*) harvester, which is originally designed to buffer its harvested energy into a supercapacitor block and provide a fixed 5 V voltage output for a target medium-power (1-10 W) embedded device. In [34], the UR-SolarCap is presented as a system comprising (i) a solar panel input, (ii) the UR-SolarCap board itself, which is a 20 cm × 12 cm Printed Circuit Board (PCB) that has

soldered RLC components, a microcontroller and other ICs (hardware), MPPT and other software programmed in the microcontroller flash ROM (firmware), and (iii) a supercapacitor block, as shown in Fig. 8, with the supercapacitor block abbreviated as “SCap” and UR-SolarCap board is abbreviated as “URSC.” This is consistent with Fig. 7, with the exception of the *Pre-conditioning* component that is necessary for wind power sources as explained in Section 6.2. Table 6 tabulates the notations that we use to describe the hybrid energy harvesters.

The designs that we introduce in this section and the following sections expand on this concept as follows; (i) they modify the power input to cover a range of hybrid options, including ones introduced in Section 5.2, (ii) they use one or more UR-SolarCap boards in their design for *single-board* and *multi-board* options, and (iii) they use the supercapacitor block in exactly the same way. Although UR-SolarCap is technically a “system,” we use the term “board” during our descriptions to refer to it in our modularized designs. Therefore, our reference to “*multi-board*” implies “*using multiple UR-SolarCap boards.*”

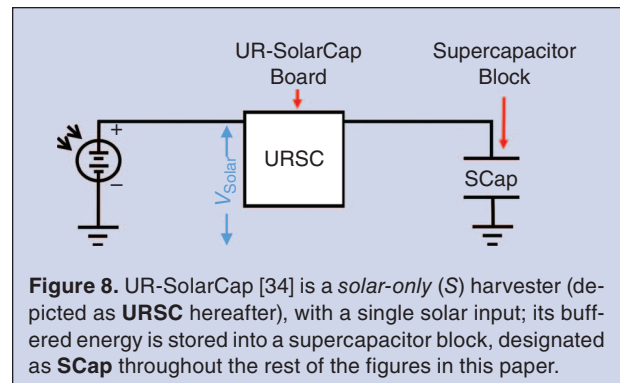


Figure 8. UR-SolarCap [34] is a *solar-only* (*S*) harvester (depicted as **URSC** hereafter), with a single solar input; its buffered energy is stored into a supercapacitor block, designated as **SCap** throughout the rest of the figures in this paper.

Table 6. Notations used to describe the hybrid energy harvesters (Sections 6 and 8), with references to which equations/sections they appear in.

Notation	Equations (Sections)	Description
$P_{\text{generator}}$	24 (6.3)	Output power of a generator
$P_{\text{harvested}}$	24 (6.3)	Power absorbed by a harvester
P_{source}	24 (6.3)	Available power at power generator
P_{cell}	24 (6.3) 25 (8.2)	Max. power can be absorbed
$P_{\text{cooperative}}$	25 (8.2)	Power harvested in <i>Cooperative</i> mode.
P_{regular}	25 (8.2)	Power harvested in <i>Regular</i> mode.

6.1. Single-Board Solar-Only (S) Energy Harvesting

UR-SolarCap can be thought of as an *S* harvester, according to the taxonomy introduced in Section 5.2. Modularity of UR-SolarCap allows us to use any type of conventional solar panel at its input, provided that the power and voltage specifications are not exceeded [34]. As its primary functionality, UR-SolarCap supervises the entire harvesting process and distributes the generated power among the load and various internal circuit devices of the system; it buffers harvested energy into the energy storage block to help reduce system downtime, as discussed in Section 4. Its firmware component executes the fractional V_{OC} method [94].

The MPPT algorithm is executed by the 8-bit PIC16F1783 microcontroller [95], which is a part of UR-SolarCap. The fractional- V_{OC} MPPT algorithm requires the continuous computation of $V_{MPP} = 0.82 \times V_{OC}$ [34]. Using a voltage sensor and an integrated ADC, the microcontroller measures the V_{OC} and keeps the solar panel voltage (V_{solar}) close to V_{MPP} ; because the harvester portion of UR-SolarCap is built by using a SEPIC DC-DC converter [96], which facilitates energy transfer from the solar panel into the supercapacitor buffer via a single duty cycle parameter (D), a higher D value increases the energy transfer rate, thereby lowering the input voltage (V_{solar}). Therefore,

when solar irradiation is higher, V_{MPP} consequently becomes higher, forcing the SEPIC converter to transfer energy at a higher rate.

In addition to its energy harvesting functionality, UR-SolarCap also provides overcharge protection, voltage regulation for internal components, a Bluetooth and RS232 communication infrastructure, and a smooth auto wake-up feature. Its communication infrastructure allows UR-SolarCap to transmit its internal system status—including the amount of energy available in the supercapacitors—to the host embedded device that is being powered from it. Its auto wake-up feature allows it to shut down for an indefinite amount of time (e.g., during multiple consecutive days with no solar power input) and resume a fully functional status at the end of this dark period. The implementation and architecture of UR-SolarCap are discussed extensively in [34].

6.2. Single-Board Wind-Only (W) Power Harvesting

In this section, we describe how a wind-only energy harvesting system (*W*) can be designed by adapting the solar-only (*S*) UR-SolarCap board; our design goal is to retain the versatility of UR-SolarCap by incorporating the auto wake-up, over voltage and over power protection, Bluetooth and RS232 communication, and a regulated 5 V voltage features. Furthermore, we introduce a new version of the PIC firmware that executes an MPPT algorithm, which is suitable for wind power sources. Implementing a *W* system proves to be more complicated than simply connecting an *S* harvester to a wind turbine, because the characteristics of wind and solar power sources are fundamentally different. Nonetheless, it is possible to reuse the UR-SolarCap hardware and software as the basis for a *W* harvester design.

The high-level architecture of our proposed *W* configuration is shown in Fig. 9. Compared to the *S* harvester, the proposed *W* harvester includes three additional hardware components: **(i)** a wind turbine to convert the mechanical wind power to electrical power, **(ii)** a rectifier to convert the three-phase AC output of the turbine to DC, and **(iii)** a 25 V voltage limiter to ensure that the UR-SolarCap voltage specifications are not exceeded. Figure 10 depicts the circuit schematic of the rectifier and the voltage limiter, which we envision as a daughter board that interfaces UR-SolarCap; this modular design eliminates the need for extensive modifications to UR-SolarCap to turn it into a *W* harvester. The voltage limiter is necessary because the voltage output of the wind turbine can reach as high as 50 V, posing a damage threat to UR-SolarCap. This contrasts with μ -power systems, such as Medical Cyber Physical Systems, which incorporate IoT components that produce voltages far below 1 V [97]–[100].

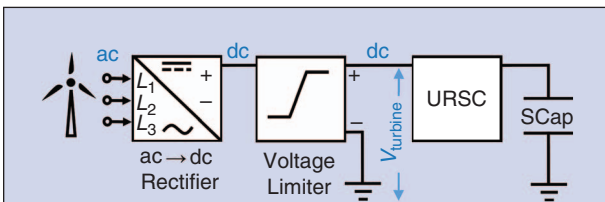


Figure 9. In the *W* configuration, the AC output of the wind turbine is first rectified and voltage-limited to comply with UR-SolarCap voltage specifications. Additionally, a new firmware effectively tracks the MPP.

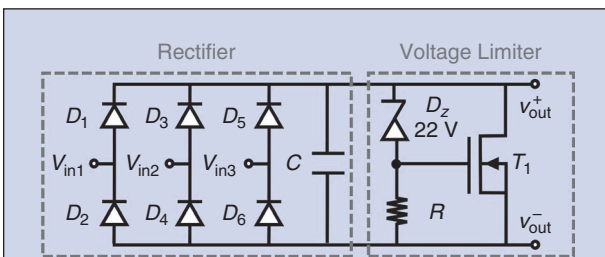


Figure 10. The output of the voltage rectifier may reach > 50 V. This circuit limits it to ≈ 25 V, which is required by UR-SolarCap. When V_{in} reaches 24–25 V, The Zener diode D_z turns on T_1 , thereby shunting the turbine and clipping its voltage. Terminal V_{in} is connected to the wind turbine. Terminal V_{out} is connected to the UR-SolarCap main board supply input.

Since the P-V characteristics of solar and wind are different, an alternative MPPT algorithm is needed for the W configuration. A variety of such algorithms has been studied in the literature [101]–[104]. Our proposed W architecture employs the well-known Hill Climbing (HC) method [105]. The implementation of the HC algorithm is simple, and does not require wind or rotational speed sensors. However, its capability to track the MPP in rapidly changing wind conditions is limited [106]. Because the S and W designs use different MPPT algorithms, a new firmware design is necessary for UR-SolarCap to allow it to work as a W harvester.

The power output of a prototype implementation of a UR-SolarCap-based W harvester—that uses a Higoo™ 50 W turbine as its wind power generator—is shown in Fig. 11 for a five-minute interval; the data is logged through the voltage and current measurement capabilities of UR-SolarCap and transmitted to a PC through its RS-232 communication module. The transmitted data is then saved as a CSV and plotted using GNU Octave [107]. Figure 11 demonstrates an interesting characteristic of wind power supply; while solar supply exhibits long periods of steady power, wind supply exhibits large peaks in short intervals.

6.3. Single-Board Single-Source Characteristics

The main advantages of the S and W configurations are their simplicity and low cost, especially in environments with high solar and wind power availability. However, single-board single-source harvesting setups are susceptible to two fundamental drawbacks: (i) the original UR-SolarCap design imposes a power limit (P_{ceil}) to avoid damage to its internal components. Therefore, even if the available power at the power generator (P_{source}) is higher than P_{ceil} , the harvested power ($P_{\text{harvested}}$) is limited to P_{ceil} by the harvester; as formulated below:

$$P_{\text{harvested}} = \min(P_{\text{source}}, P_{\text{ceil}}), \quad (24)$$

which can lead to substantial waste when $P_{\text{source}} \gg P_{\text{ceil}}$. Moreover, (ii) as mentioned previously, reliance on a single energy source restricts the applicability of a field system to locations where solar or wind energy are continuously available. In the following sections, we introduce harvesting configurations that can utilize hybrid power sources.

7. Hybrid Harvesting Systems

In this section, we introduce three distinct hybrid (multi-source) harvesting system architectures that can harvest and buffer a combination of solar and wind power sources.

(i) **Independent Multi-Board harvesting:** This architecture incorporates *multiple non-communicating*

harvesting boards, each responsible for harvesting a single power source. We expand our taxonomy introduced in Section 5.2 to cover the configurations in this category; for example, SWW refers to an independent multi-board configuration that includes one solar panel and two wind turbines. We provide an overview of this category in Section 7.1.

(ii) **Cooperative Multi-Board harvesting:** This architecture incorporates *multiple communicating* harvesting boards, where each board not only harvests its own power source, but also communicates with the other boards for improved efficiency, fault tolerance, and extended power range. S_2S_2 is an example of this category, where two harvesting boards communicate to jointly harvest two solar sources. We provide a high-level overview of cooperative multi-board harvesting in Section 7.2; furthermore, a detailed operational analysis of this category is provided in Section 8.

(iii) **Time-Multiplexed Single-Board harvesting:** This architecture employs a single harvesting board, which can receive power from two or more sources through an analog multiplexer; each multiplexed input is harvested only a fraction of the time, hence our naming *time-multiplexed*. An example notation “ $S \parallel W \parallel W$ ” refers to an architecture in this category that receives one solar and two wind power sources as input. We provide an overview of this architecture in Section 7.3 and a detailed operational analysis in Section 9.

7.1. Independent Multi-Board Harvesting

In this architecture, the outputs of multiple single-source harvesters (i.e., S or W configurations) are connected

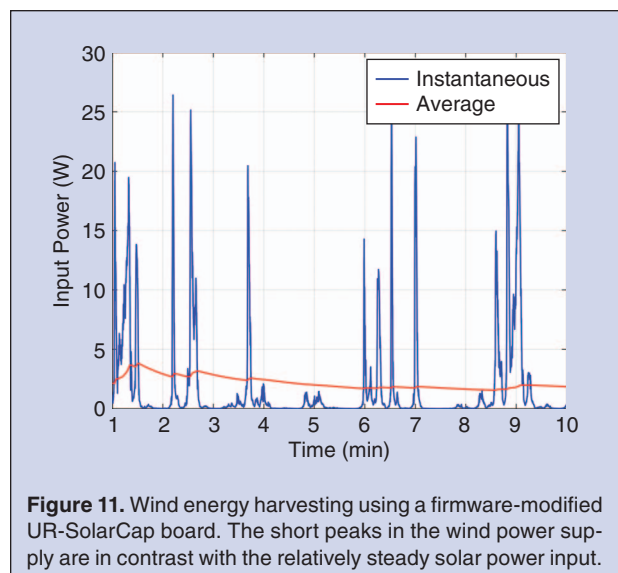


Figure 11. Wind energy harvesting using a firmware-modified UR-SolarCap board. The short peaks in the wind power supply are in contrast with the relatively steady solar power input.

to the same supercapacitor block. While each harvester receives its input power from a different source, its harvested energy is stored in a shared supercapacitor block. Representative configurations of this family are shown in Fig. 12; for example, the *SWW* configuration in Fig. 12(e) utilizes three separate UR-SolarCap boards to harvest one solar and two wind power sources independently and the harvested energy is buffered in a single supercapacitor block to power an embedded device.

In the *SS* and *SSS* configurations, two or three separate solar panels provide power into the system. Although these two configurations use the same type of power source, they can still be considered as hybrid power sources, because installing them at different locations and orientations can produce a complementary power input; for example, for two solar panels facing the sun at different angles, the power can increase at one solar panel when it decreases at the other [108]. A similar argument for the *WW* and *WWW* configurations can also be made; for example, in mountainous areas, multiple wind turbines—placed at different physical locations—can provide complementary characteristics.

In comparison to other hybrid architectures, simplicity is the main advantage of independent multi-board harvesting. Because of the independence of the harvesters, this configuration is highly scalable; adding a new power input (e.g., going from *WW* to *SWW*) is just the matter of adding another UR-SolarCap and connecting its input to the new power source (*S* in this example)

and its output to the shared supercapacitor block. Furthermore, this scalability can be used to provide fault tolerance to the system; if one of the harvesters fails, the others continue harvesting energy, thereby avoiding a total system shutdown.

7.2 Cooperative Multi-Board Harvesting

The cooperative multi-board harvesting architecture consists of two single-source (*S* or *W*) harvesters that communicate through a link to coordinate their operation. Figure 13 depicts the configurations in this category; the communication link—used in cooperation during harvesting—is denoted as “COM” in Fig. 13. Each UR-SolarCap board has an upper limit in the amount of power it can harvest, denoted as P_{ceil} ; the internal firmware over-power protection prevents a UR-SolarCap board from harvesting a higher amount of power to avoid circuit damage. The cooperation mechanism introduced in this category allows two boards to harvest $2\times$ the amount of power of a single board. To achieve this, an analog multiplexer is placed between each power source and UR-SolarCap board, allowing that power source to be channeled into one of the UR-SolarCap boards; a selection logic, determined as a function of the cooperation mechanism, enables this architecture to be used in one of two operational modes: *Regular* and *Cooperative*.

In *Regular* mode, which is the system default, the system operates as an independent multi-source configuration, in the way described in Section 7.1,

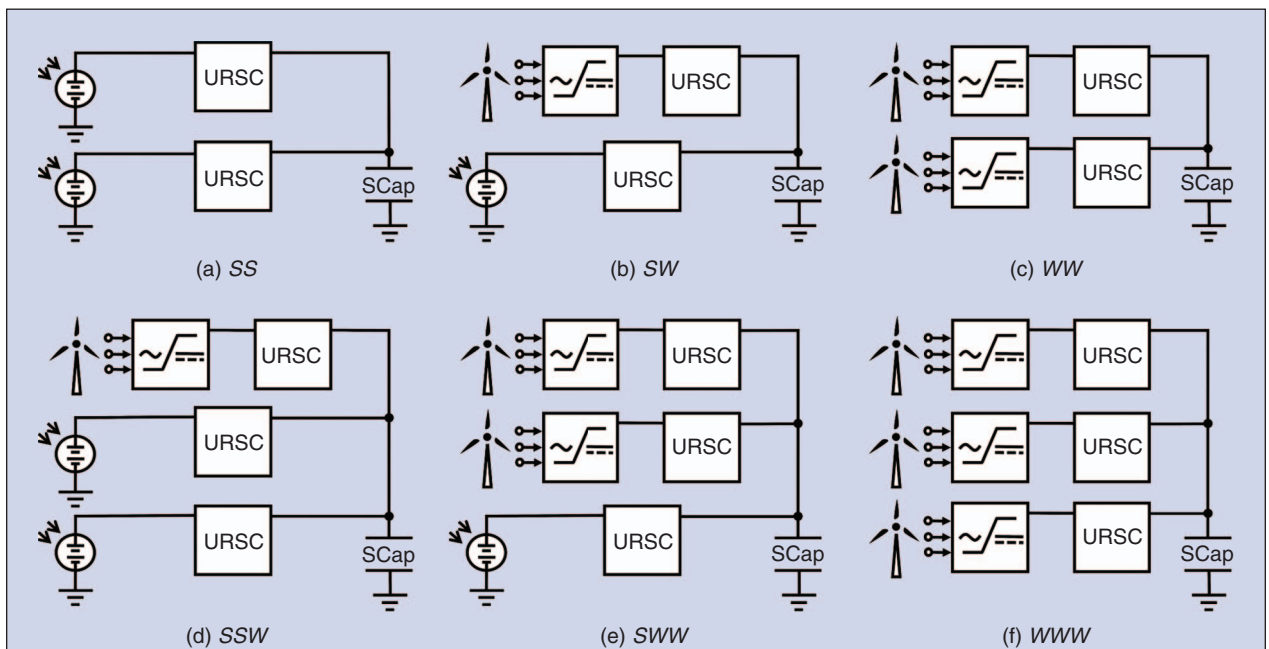
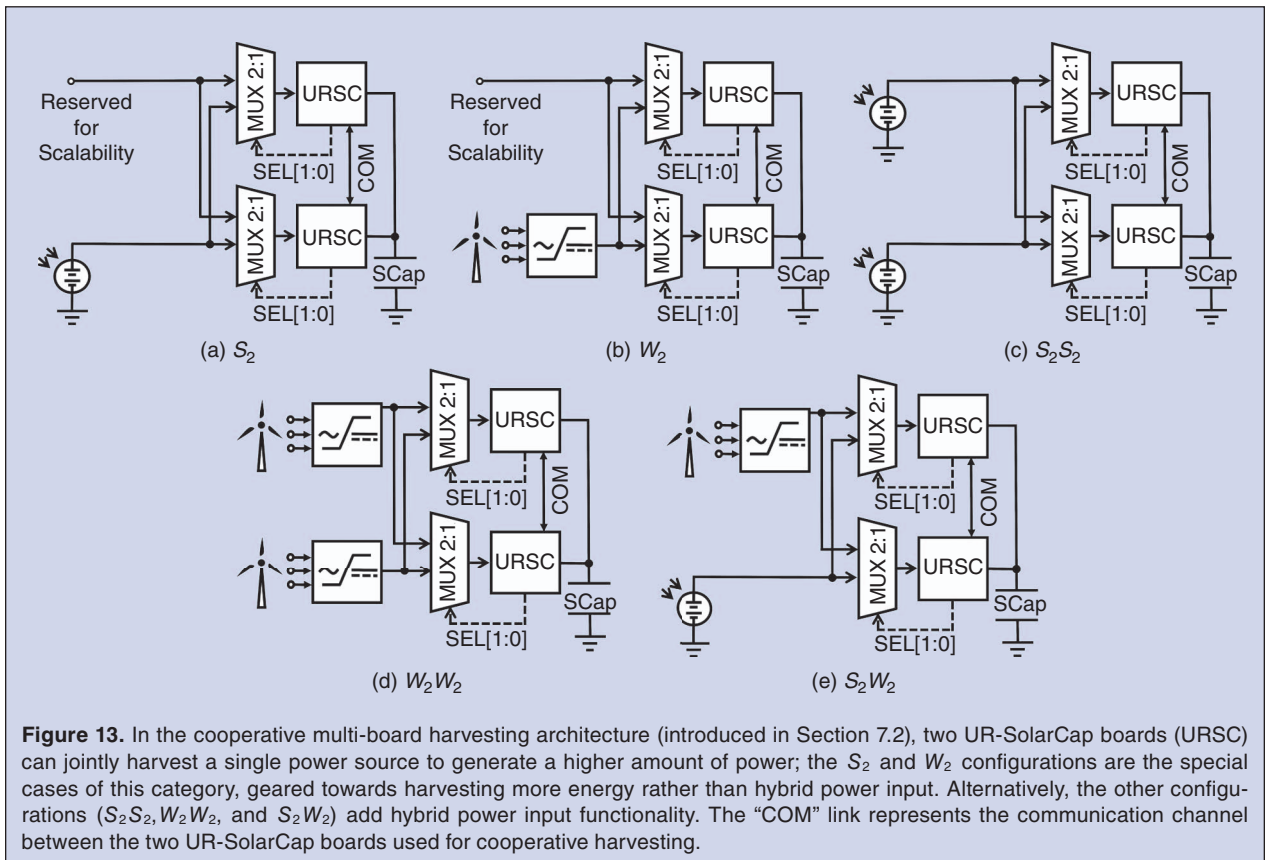


Figure 12. A high-level overview of independent multi-board harvesting configurations that we introduce in Section 7.1. The UR-SolarCap board is denoted as “URSC,” which receives its input from one or more solar/wind power sources and buffers its harvested energy into a supercapacitor block, which is denoted as “SCap.”



by selecting the multiplexers to channel each power input to its corresponding harvester. In case one of the boards has a higher amount of power available at its input than P_{ceil} , it communicates this status to the second board; the second board then joins efforts to harvest the same input cooperatively, by selecting its multiplexer to channel that power input to itself. This mode, where a single power input is channeled into two harvesters, is called the *Cooperative* mode, during which both harvesters use the COM link to adjust their duty cycles to harvest an equal portion of the available power input. We provide the implementation details of this mode in Section 8.

S_2 and W_2 options include a single power source, which is jointly harvested by two boards, whenever the system operates in *Cooperative* mode. In *Regular* mode, however, one board harvests its power source and the other one remains idle. Rather than being a hybrid system, S_2 and W_2 are used in cases where solar panels and wind turbines provide power inputs that are too high for a single board to handle; in these cases, the system always operates in *Cooperative* mode, thereby avoiding a waste of resources. In *Regular* mode, S_2S_2 , W_2W_2 , and S_2W_2 configurations operate as *SS*, *WW*, and *SW* harvesters, respectively. In *Cooperative* mode, the power

source that provides a lower amount of power is disconnected from the system using the multiplexer, while the other source is jointly harvested by both boards by distributing the input power to them evenly.

Among all of our proposed hybrid architectures, cooperative multi-board is the only one that addresses the power limitation (P_{ceil}) of the S and W configurations. Assuming that the both boards in this configuration are identical, the harvesting power limit of the entire system reaches $2 \times P_{\text{ceil}}$. Moreover, similar to independent multi-board harvesting configurations, described in Section 7.1, cooperative multi-board harvesters offer fault-tolerance through hardware redundancy. However, as we discuss in Section 8, *Cooperative* mode adds to the system complexity in terms of both the hardware and firmware. Although we only describe and report on experiments for this category with two harvesters, an expansion to ≥ 3 boards is possible.

7.3. Time-multiplexed Single-Board Harvesting

Although the hardware redundancy and the increased power limit, offered by the previous two categories, is preferable in applications where cost is not of primary concern, we propose the time-multiplexed single-board harvesting architecture for cost sensitive applications.

Harvesters in this category utilize a single harvesting board to simultaneously harvest multiple power sources. As depicted in Fig. 14, every configuration in this category consists of **(i)** two or more power sources, **(ii)** an analog multiplexing mechanism, **(iii)** a single harvesting board, and **(iv)** a supercapacitor-based energy buffer. The solar and wind power inputs are connected to the harvesting board through the analog multiplexer, which is controlled by the firmware; the firmware cycles through the available power inputs in a round-robin fashion by connecting a single input at any point in time and disconnecting the others. While a power source is disconnected, its generated energy is buffered in a small capacitor. When connected, the harvester treats the small capacitor as the power source and harvests from it during the allocated time slot for that source; in this way, the harvesting process is *time-multiplexed*. A detailed analysis of the time-multiplexed single-board harvesting category is presented in Section 9.

The primary advantage of this category is its reduced costs and potentially reduced system size due to the elimination of multiple boards. Furthermore, expansion to multiple power sources using this category is fairly straightforward. However, this category suffers from a potentially increased hardware failure rate, due

to the harvesting board being a single point of failure in the system.

7.4. Comparison of Harvesting Architectures

A comparative summary of all harvesting architectures introduced in this section is tabulated in Table 7. Overall, due to its simplicity and fault tolerance, independent multi-board harvesting is suitable for fast deployment of mission-critical systems. Cooperative multi-board harvesting is recommended, if the nominal power of an existing power transducer such as a solar panel or wind turbine exceeds the harvesting capability of the harvesting board. This is a common design practice, as system designers are occasionally compelled to tradeoff cost for system availability to meet the worst-case scenario requirements. In normal scenarios, however, cooperative multi-board harvesting can harvest the surplus portion of energy to support auxiliary functionality. Time-multiplexed single-board harvesting is suitable for large-scale systems, in which fault tolerance is not a requirement. The expandability of this architecture also adds to system flexibility by allowing each harvesting node to be modified based on the power requirements driven by desired new functionality.

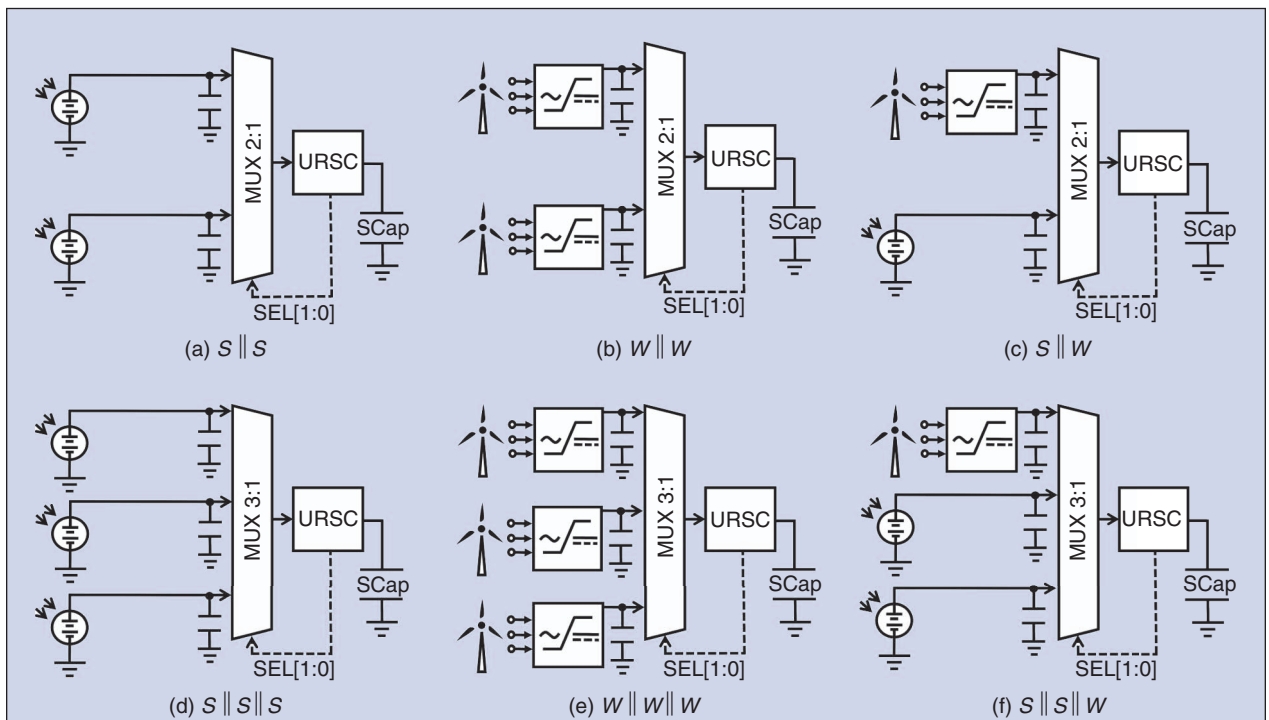


Figure 14. Some example configurations of the time-multiplexed single-board harvesting system (introduced in Section 7.3); in all of these configurations, a single harvesting board concurrently harvests multiple power sources. When a power source is not connected to the harvesting board, its generated power is buffered in intermediary capacitors, inserted between the power source and the analog multiplexer (which are termed *input buffer capacitors*). In this figure, URSC box designates the harvesting board and SCap represents the supercapacitor-based energy storage block.

Table 7.

Example configurations of hybrid harvesters proposed in the paper, along with the section each configuration is described in and its associated figure. Each (•) represents a single power source included in the configuration; for example, *SS* harvester incorporates two separate solar power sources. *Board Count* represents the number of UR-SolarCap harvesting boards in each configuration.

Type	Sec.	Notation	Sources		Board Count	Fig.
			S	W		
Independent Multiple Board	7.1	<i>SS</i>	••		2	12(a)
		<i>SW</i>	•	•	2	12(b)
		<i>WW</i>		••	2	12(c)
		<i>SSW</i>	••	•	3	12(d)
		<i>SWW</i>	•	••	3	12(e)
		<i>WWW</i>		•••	3	12(f)
Cooperative Multiple Board	7.2	S_2	•		2	13(a)
		W_2		•	2	13(b)
		$S_2 S_2$	••		2	13(c)
		$W_2 W_2$		••	2	13(d)
		$S_2 W_2$	•	•	2	13(e)
Time Multiplexed Single Board	7.3	$S \parallel S$	••		1	14(a)
		$W \parallel W$		••	1	14(b)
		$S \parallel W$	•	•	1	14(c)
		$S \parallel S \parallel S$	•••		1	14(d)
		$W \parallel W \parallel W$		•••	1	14(e)
		$S \parallel S \parallel W$	••	•	1	14(f)

**8. Hardware/Firmware Implementation:
Cooperative Multi-Board Harvesting**

In this section, we detail the implementation of cooperative multi-board harvesters introduced in Section 7.2, which are composed of five components: **(i)** two single-board single-source harvesting boards, **(ii)** a communication channel to allow the two boards to communicate, **(iii)** a shared supercapacitor-based energy buffer, **(iv)** one or more power inputs that are cooperatively harvested by these boards, and **(v)** an analog multiplexer per board to channel the power sources into these boards in a variety of configurations, determined by the harvesting mode. Whenever we are referring to configurations with multiple boards, we denote them as Board₁, Board₂, etc. With respect to hardware, the two harvesting boards utilized in cooperative multi-board harvesters are identical to the *S* and *W* configurations. However, their software operation differs based on the mode that they are currently operating in (*Regular* and *Cooperative*, as discussed in Section 7.2).

In this section, we explain the implementation details of the hardware and software components of cooperative multi-board harvesters.

8.1. Analog Input Multiplexing Circuitry

The analog multiplexer, connected to the input of each harvesting board, allows the channeling of one or two power sources into the harvester. In the S_2 and W_2 configurations (Figs. 13(a) and 13(b)), although a simple switch will suffice, they are indicated by 2:1 MUXes, where one input is not connected to any power source; instead, it is reserved for connecting a power source in the future. This depiction generalizes this category; an additional power source can be readily connected to the available reserved MUX input for scalability. Configurations with two power sources such as $S_2 W_2$ or $W_2 W_2$ (Fig. 13(e) and Fig. 13(d)), also use 2:1 MUXes.

An implementation of analog multiplexing functionality using N channel and P channel MOSFETs is depicted in Fig. 15, where the inputs *SRC1* and *SRC2* are connected

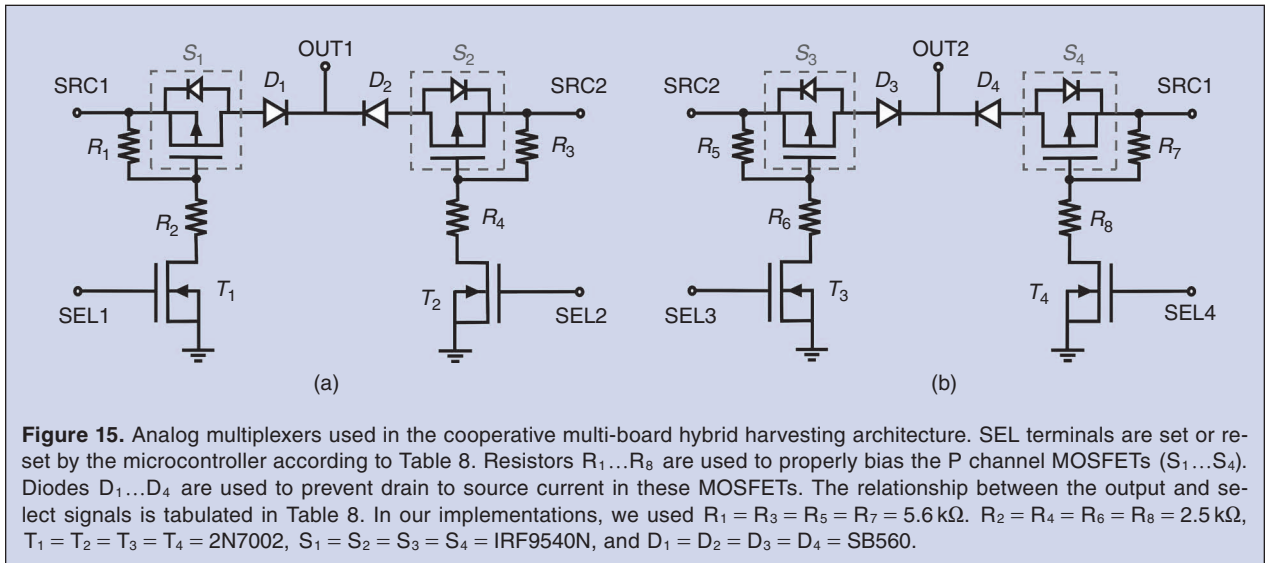


Table 8.
The relation between the output and select signals of the multiplexers in the cooperative multi-board harvesting architecture. “SELECT” represents the four control signals denoted by SEL1, SEL2, SEL3, and SEL4 in Fig. 15. “Not Allowed” combinations should be avoided, because they are either unsupported by the hardware or are undefined in the firmware. The SRC1 and SRC2 inputs are the primary sources of harvesting Board₁ and harvesting Board₂. Combination 1010 is *Not Allowed*, because in cooperative multi-board harvesting, at least one of the harvesting boards must harvest its primary power source.

SELECT	OUT1	OUT2	Mode
0000	HI-Z	HI-Z	OFF
0001	SRC1	HI-Z	Regular
0010	SRC2	HI-Z	Not Allowed
0011	X	HI-Z	Not Allowed
0100	HI-Z	SRC2	Regular
0101	SRC1	SRC2	Regular
0110	SRC2	SRC2	Cooperative
0111	X	SRC2	Not Allowed
1000	HI-Z	SRC1	Not Allowed
1001	SRC1	SRC1	Cooperative
1010	SRC2	SRC1	Not Allowed
1011	X	SRC1	Not Allowed
11XX	X	X	Not Allowed

to the power sources. Their outputs, *OUT1* and *OUT2*, are connected to the harvesting boards. The channeling of the power sources into the *SRC* inputs of each multiplexer is achieved by a four-bit selection signal as shown

in Table 8. Each power source can be channeled into Board₁, Board₂, or left disconnected (Hi-Z). For example, in *Regular* mode, the 0101 selection vector establishes the *SRC1* → *OUT1* and *SRC2* → *OUT2* connections, thereby allowing Board₁ to harvest the first power source and Board₂ the second. Alternatively, when the power level at *SRC2* becomes much higher than *SRC1*, the firmware enters the *Cooperative* mode and selects the 0110 vector, establishing the *SRC2* → *OUT1* and *SRC2* → *OUT2* connections; in this case, both Board₁ and Board₂ cooperate towards harvesting an equal portion of the available power. The firmware is designed to never select one of the “Not Allowed” conditions, because they may cause hardware malfunction.

The multiplexing mechanism works as follows: Applying a “0” to any one of the SEL inputs turns off the corresponding N channel MOSFET; in a short time period after this, the P channel MOSFET—acting as a switch—turns off. For example, applying SEL1=0 turns off T_1 and causes the charge in the C_{GS} of the P channel MOSFET—depicted as S_1 in Fig. 15—to drain and its $|V_{GS}|$ go down to $|V_{GS}| = 0\text{V}$, thereby turning it off. The amount of time that it takes between setting the SEL1=0 to the time when S_1 is totally turned off is determined by the RC constant of R_1 and the input capacitance of S_1 .

To turn S_1 back on, SEL=1 must be applied, which will re-charge the C_{GS} of S_1 in an RC constant determined by the input capacitance of S_1 , as well as the R_1, R_2 pair. The voltage drop across these resistors results in $V_{GS} < 0\text{V}$, which turns on the P channel MOSFET and sets its output voltage approximately equal to its source voltage. Depending on the voltage of the connected source, the voltage of the output might exceed the disconnected source voltage. Even if the P channel MOSFET is off, some

current might still flow from the output to the source through the transistor's body diode. Diodes D_1 and D_2 are added to the design to prevent the reverse current from output to the source ports in these situations.

8.2. Cooperation Mechanism

We use the term *cooperation mechanism* to refer to the platform that allows the boards to communicate and coordinate their harvesting operation. This mechanism involves two layers: **(a)** a hardware-implemented physical layer and **(b)** a firmware-controlled layer. The physical layer is composed of two serial data communication wires, RX and TX. As there are only two harvesting boards in cooperative multi-board configurations, no advanced networking services such as access management and node addressing is required. However, if the architecture needs to be adapted to include more than two harvesting boards, more sophisticated communication protocols (e.g., SPI and CAN) can be utilized. The firmware layer includes a simple control protocol for the two boards to synchronize their harvesting; this protocol manages the physical layer and allows the two boards to determine when to initiate/terminate/accept/reject the *Cooperative* mode.

In cooperative multi-board harvesting, the firmware of each harvester starts its operation in *Regular* mode and is responsible for determining when to switch to *Cooperative* mode; when the power level at a source increases to beyond P_{ceil} , each board requests the other to join its efforts to harvest this source cooperatively, through a four-stage handshake protocol: **(i)** the initiator (Board₁) first sends a request by setting its TX channel, **(ii)** Board₂ suspends its MPPT if its input power is below a threshold and switches its power source by placing the proper MUX select signals; it provides an acknowledgment to Board₁ by setting its TX pin (which is connected to RX pin of Board₁), **(iii)** once its RX pin is set, Board₁ enters the *Cooperative* mode and clears its TX pin (which is connected to RX pin of Board₂), and **(iv)** finally, Board₂ begins the *Cooperative* mode as soon as its RX pin is cleared. To eliminate ambiguity, we refer to Board₁ as *master* and Board₂ as *slave*. When both boards are in *Cooperative* mode, the master determines the right value of the duty cycle and shares it with the slave through the communication channel. This approach guarantees that the harvesting load on both boards is equal because their duty cycles are identical.

Although simple, this suggested cooperation mechanism may fail to increase the overall amount of harvested power in multi-source cooperative configurations (S_2S_2, S_2W_2, W_2W_2). This limitation is shown by Eq. 25, which compares the range of instantaneous delivered power in cooperative configurations operating in *Coop-*

erative ($P_{\text{cooperative}}$) and *Regular* (P_{regular}) modes. Assuming that the cooperation threshold is set to P_{ceil} , the total amount of harvested power cannot fall below this value when the system is in *Cooperative* mode. As Eq. 25 implies, it is possible that P_{regular} exceeds $P_{\text{cooperative}}$ (because they overlap), which means that the system is worse off by sustaining the *Cooperative* mode in some situations. This is a condition when the master decides to terminate the *Cooperative* mode; the most straightforward approach is to exit this mode if the harvested power of each board is lower than half of the P_{ceil} .

$$\begin{aligned} P_{\text{ceil}} \leq P_{\text{cooperative}} \leq 2P_{\text{ceil}}, \\ 0 \leq P_{\text{regular}} \leq 2P_{\text{ceil}}. \end{aligned} \quad (25)$$

However, as it is evident from Eq. 25, terminating cooperation even when the input power exceeds half of the P_{ceil} might increase the harvested power in some cases. One solution to this problem is to set higher values for the threshold. This, however, reduces the duration in which the system operates in the *Cooperative* mode. Another solution is to continually log the harvested power and use the history of the system to predict the incoming power in near future. Both master and slave can then decide to enter or leave cooperation based on their expectations of changes in the incoming power. The efficacy of this solution is completely dependent on the accuracy of the power forecasting. Therefore, for sources such as solar power, which are generally stable and predictable, this approach is compelling. However, predicting the wind pattern using the past data proves to be quite challenging.

8.3. Single Source, Multi-Board Configurations

The S_2 and W_2 setups include only a single power source, which effectively makes them single-source energy harvesters. In both configurations, the specifications of power sources, particularly the output voltage, should comply with UR-SolarCap original requirements. However, due to the option of cooperative harvesting, the system can harvest up to twice the amount of UR-SolarCap power limitation (P_{ceil}).

8.4. Multiple Source, Multi-Board Configurations

In S_2S_2 , the panels are typically set up in different orientations to provide a more steady supply of harvestable energy as the relative location of sun in the sky varies. Because the performance of solar panels is highly dependent on the direction of the incident light [108], the enhancement in efficacy provided by double-panel harvesting should not be underestimated. Similarly, two wind turbines placed in different locations can be simultaneously harvested in W_2W_2 configuration. It is also possible to harvest two power source types in

S_2W_2 setup. The design of multiplexers is identical in S_2S_2, W_2W_2 , and S_2W_2 configurations. Two 2:1 analog MUXes are included to provide a path among all the harvesting boards and power sources. All the other hardware and software components remain unaffected as well. The board that executes the HC MPPT algorithm in its firmware should harvest wind energy as its primary source, while the harvesting board executing fractional open-circuit voltage MPPT method should primarily harvest solar energy. Each board harvests its primary power source in *Regular* mode and can initiate the *Cooperative* mode if the output of its primary source exceeds the pre-defined threshold.

The communication protocol of cooperation mechanism limits the system's scalability to two harvesting boards. However, with additional adaptations in the multiplexer design and communication protocols, this architecture can be adapted to include more power sources. Particularly, S_2S_2 and W_2W_2 can be combined into a triple source harvesting, operating as either $S_3S_3W_3$ or $S_3W_3W_3$ systems. In this case, 2:1 multiplexers should be replaced by 3:1 multiplexers. Furthermore, an addressing protocol should be implemented in the system, making each board separately addressable. An I^2C protocol can meet this requirement well. Once implemented, triple source cooperative harvesting not only lowers the system's downtime due to higher number of included power sources, but also increases the system's power limit to $3 \times P_{\text{cell}}$, when all boards have an identical P_{cell} power limit.

9. Hardware/Software Implementation: Time-Multiplexed Single-Board

In this section, we detail the implementation of time-multiplexed single-board harvesters introduced in Section 7.3. Harvesters of this category have a significant cost advantage because they only require a single UR-SolarCap board to harvest more than one power source. However, due to that single board being a single point of failure, designs in this category suffer a reliability and fault-tolerance disadvantage.

9.1. Time-Multiplexing Mechanism

All of the power sources are connected to a single harvesting board through an $n:1$ analog MUX, where n is the number of power sources. Voltage limiters and rectifiers are required if the power source voltage does not comply with UR-SolarCap specifications (Section 6.2). Unlike the cooperative multi-board architecture, the included power sources in a time-multiplexed configuration are not connected/disconnected based on their power availability; instead, the harvesting board periodically switches between them—in a round robin

fashion—at a pre-defined frequency (f_{sw}). In summary, a time-multiplexed harvester is a polymorphic system that periodically changes between S and W configurations; from the perspective of the harvesting board, the system harvests a single power source at every instant of time, similar to S and W setups.

9.2. Analog Input Multiplexing Circuitry

Analog MUXes used in time-multiplexed single-board and cooperative multi-board architectures are identical, although their operation differs as follows. In cooperative multi-board harvesting, the multiplexer operation is controlled based on the power availability of each source, while in time-multiplexed single-board systems, the switching occurs periodically regardless of the power level of each source. An $n:1$ multiplexer is required for a time-multiplexed harvester, harvesting n power sources. For this design, the same 2:1 MUX shown in Fig. 15 can be utilized; on the left side of Fig. 15, a 2:1 MUX is constructed from two separate analog switches that connect $SRC1$ and $SRC2$ to the same output ($OUT1$). This circuit is highly scalable by using the same (N channel– P channel– R – D) building block and connecting a new input (e.g., $SRC3$) to the same output ($OUT1$) to build a 3:1 MUX. Similarly, a fourth repetition of the same building block implements a 4:1 MUX, connecting $SRC4$ to $OUT1$, etc. An $n:1$ MUX requires n repetitions of the same building block.

9.3. Firmware to Implement Time-Multiplexing

The firmware of time-multiplexed single-board harvesting systems performs two additional tasks compared with other architectures. First, it controls the multiplexer to periodically switch among all available power sources. The firmware also executes the proper MPPT algorithm according to the type of each connected power source. The switching process is accomplished using a selection vector, composed of $SEL1, SEL2, \dots$ signals (Fig. 15). To assure proper operation, the round robin sequencing among available power sources is accomplished by first disconnecting the currently-in-use power source and then connecting the next. More sophisticated sequencing algorithms than round robin can also be implemented—such as priority-based queuing and interrupt-based selection—according to application requirements. Before disconnecting a power source, the firmware saves a snapshot of its MPPT algorithm execution status. Whenever that source is reconnected, its MPPT status is retrieved and the firmware continues the MPPT procedure from that point. Although the MPPT status of a power source changes during its disconnection period, this retrieval of its previous MPPT status substantially improves the firmware efficiency by reducing the MPPT

algorithm delay. This is particularly beneficial for configurations that incorporate one or more wind power sources, because wind turbines have a significant MPP convergence delay.

9.4. Harvesting Power Limit

The time-multiplexed harvesting architecture can harvest multiple power sources simultaneously, nonetheless the power limit for each source is still P_{ceil} . Furthermore, since there is only one harvesting board in this configuration, the total charging power of the supercapacitor block cannot exceed P_{ceil} . This contrasts with the cooperative multi-board architecture, in which the power limit is $2 \times P_{\text{ceil}}$ and the independent multi-board configuration—using n harvesting boards—with a power limit of $n \times P_{\text{ceil}}$.

9.5. Multiplexing Efficiency

The non-ideality of the MOSFET switches that are used in the input analog MUX and ripples around V_{MPP} also impact the efficiency of the time-multiplexed configurations. MOSFET power dissipation can be categorized into *resistive*, *transient*, and *switching* losses. *Resistive power losses* are determined by $R_{\text{DS(on)}}$ and V_{MPP} of the currently connected power source. *Transient power dissipation* occurs during ON→OFF and OFF→ON transitions and is proportional to the drive capability of the switching transistor that the input MUX consists of. *Switching power losses*, on the other hand, are typically negligible due to a low switching frequency (333 Hz) and small number of power transistors (two power transistors for a double-source time-multiplexed harvester). Our analysis and observation confirmed that $\eta_{\text{mux}} \approx 95\%$ in the worst-case scenarios.

Apart from the power consumption of the multiplexer, the fluctuations around V_{MPP} also have a negative impact on the efficiency of time-multiplexed harvesting configurations (η_{sw}). We can assess the percentage of voltage fluctuations in the worst case scenario [53]. If the size of the capacitors inserted between the source and the switch is 4700 μF , the switching frequency is 333 Hz, and $I_{\text{charge}}^{\text{max}} = 3.48$ A, the voltage of the input buffer ripples ± 1.11 V. Assuming $V_{\text{MPP}} = 13$ V, we calculate the ripples to be around 8.5%. This corresponds to an $\eta_{\text{sw}} \approx 0.95$ (95%), based on the study in [51].

9.6. System Modularity and Expandability

The modularity of the time-multiplexed design ensures its expandability. Adding new power sources to the time-multiplexed harvesting architecture requires a simple modification in the analog MUX by adding a (NMOS–PMOS–R–R–D) building block to the circuit shown in Fig. 15 (see Section 9.2). Whenever a new power source is

added, the firmware should be notified of its type and its harvesting order in the round-robin scheme; typically, this requires a simple update in the embedded C code, recompiling and reflashing the firmware. Theoretically, any number of power sources can be used in time-multiplexed harvesting architecture. However, having too many sources increases the time interval during which a power source remains disconnected, thereby necessitating larger input capacitors and/or a faster switching frequency to prevent large ripples around V_{MPP} , as explained in Section 9.1. Arbitrary increases in the input buffer capacitance and/or the frequency are, however, also not practical. Furthermore, adding extra power sources without increasing the power limit of UR-Solar-Cap (P_{ceil}) can saturate the amount of power transferred to the supercapacitor buffer, thereby hindering the normal operation of the system, unless the excess portion of the power can be consumed by the embedded load.

10. Experiments

In this section, we provide experimental results for a set of representative architectures in family of harvesters described in Sections 7, 8, and 9. We introduce our experimental test bench setup in Section 10.1. Our experiments are conducted at a University of Rochester ECE building through long-term measurement and logging of solar/wind patterns and operation of our harvesters. In Section 10.2, we provide the results for auto wake-up functionality of our W harvester, followed by our evaluation of the SW harvester, which is a configuration representative of independent multi-board harvesting discussed in Section 10.3. To demonstrate the operation of our cooperative multi-board harvesters, we provide experimental results for solar (S_2S_2) and wind (W_2W_2) power sources in Sections 10.4 and 10.5, respectively. Our time-multiplexed single-board harvesting results for the $S\parallel S$ configuration are presented in Section 10.6. Table 9 lists configurations on which we have conducted experiments along with the sections where each topology is introduced and the results are presented.

10.1. Experimental Setup

The experimental setup for hybrid solar/wind energy harvesting with two UR-SolarCap boards is illustrated in Fig. 16. The wind turbine is used as the wind power source, while one or more solar panels are used as the solar power source, depending on the power requirement. The multiplexer board provides separate voltage connections for two UR-SolarCap boards, which communicate with each other through dedicated RX/TX wires and control the switches on the multiplexing board through additional wires. We provide the details of different components used in our experimental setup below:

Table 9.

List of the configurations used in our experiments section/figure numbers where the corresponding results are presented.

Harvester Configuration			Results	
Notation	Section	Description	Figure	Section
W	6.2	Wind-only wake up	17	10.2
SW	7.1	Solar and wind Independent	18	10.3
$S_2 S_2$	8	Two Solar Panels Cooperative (Independent SEPIC duty cycle computation)	19	10.4
		Two Solar Panels Cooperative (Master-Slave)	20	
$W_2 W_2$	8	Two Wind Turbines Cooperative	21	10.5
$S \parallel S$	9	Two Solar Panels Time-multiplexed	22	10.6

Wind turbine: The nominal specifications of the wind turbine are 50 W and 12 Vrms (AC). However, the rectified DC voltage can reach as high as 40 V under no load condition, necessitating the use of a voltage limiter to prevent damage to the UR-SolarCap and multiplexer board.

Solar Panels: A set of solar panels with different rated voltages are shown in Fig. 16. In our experiments, a parallel configuration of multiple solar panels was used to provide the required solar power for each experiment; for example, two 30 W solar panels were connected in parallel to provide a 60 W rated power. The experiments were carried out between October and December in the Rochester, NY area. Due to relatively low solar irradiation during that period, we had to place two solar panels in parallel. The solar panels have a maximum open

circuit voltage of 24 V, which is less than the maximum allowed input voltage of UR-SolarCap.

Supercapacitor block: consists of 8×3000 F serially connected supercapacitors with a maximum rated voltage of 2.7 V each. UR-SolarCap firmware features an over-voltage protection by stopping energy harvesting when the supercapacitor block voltage exceeds $8 \times 2.7 = 21.6$ V.

Electronic load: is a programmable current sink, which is used to discharge the supercapacitor block when the block is charged to full capacity. The sink current is usually set to 7 A to discharge supercapacitors in a relatively short period while preventing the wire connections from overheating.

Pickit 3: is a programming device, which uploads a new firmware—from a HEX file—into the microcontroller’s

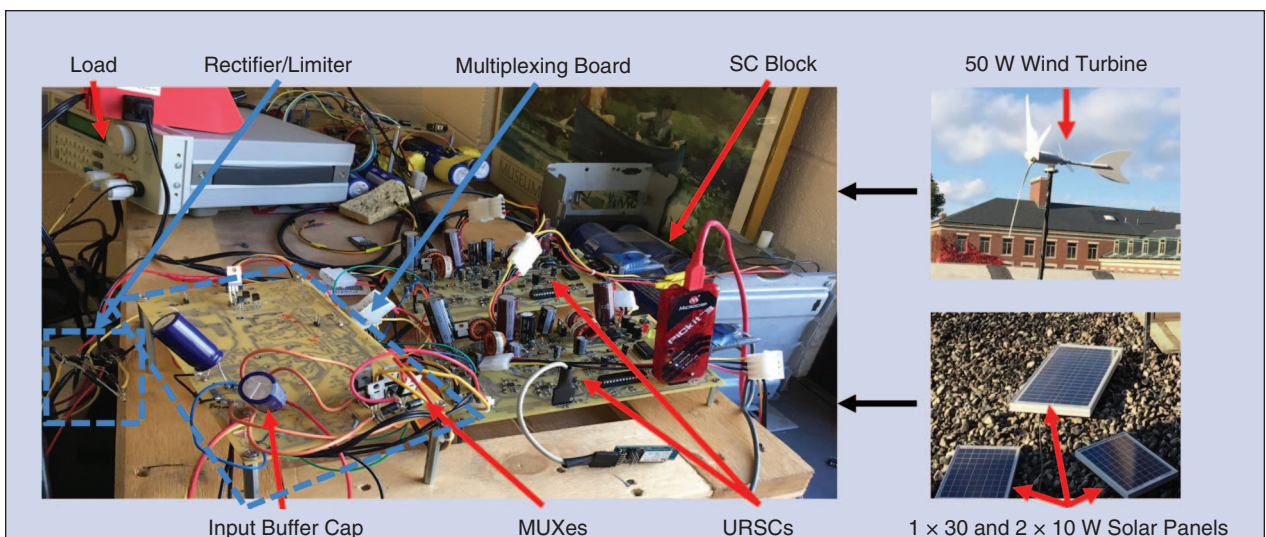


Figure 16. The experimental hybrid (solar/wind) harvesting setup (Fig. 14) used to provide the proof-of-concept results in this paper. A 50 W wind turbine is stabilized by mounting it on a pole that attaches to a wood panel on the bottom; this pole passes through a hole that is drilled on a desk. To avoid vibration, the pole is fixed by multiple screws that attach it to the desk. This setup is capable of providing experimental results for a wide range of the hybrid configurations introduced in this paper.

flash ROM inside the UR-SolarCap board, when the supercapacitor block voltage is higher than 3.5 V. Below 3.5 V, the SEPIC regulator that provides 5 V to the microcontroller is not functional, thereby preventing both the microcontroller and its programming capabilities to be operational.

Data Logging: UR-SolarCap measures the input voltage and input current of its power source, as well as the supercapacitor block voltage and transmits this information through its RS-232 port. Although the original data transmission period is set to three minutes in the UR-SolarCap firmware, we modified the firmware to decrease this period to 7 ms for finer temporal data resolution in our experimental investigations. We also included the instantaneous SEPIC duty cycle value D in the transmitted information.

The logged data by the UR-SolarCap boards is used to analyze the system performance in all of the experiments except for the *wakeup functionality* (Section 10.2) and the $S||S$ configuration (Section 10.6). For the $S||S$ experiment (Section 10.6), because we needed a sampling frequency that is much higher than the capability of the built-in PIC ADC in UR-SolarCap, we used an Agilent MSO-X 2024A oscilloscope to log solar panel voltages. In the wakeup functionality experiment (Section 10.2), because the system starts from a totally depleted energy state and the logging feature of UR-SolarCap is not available, we used Agilent 1272 DMMs (sampling rate of 1 second).

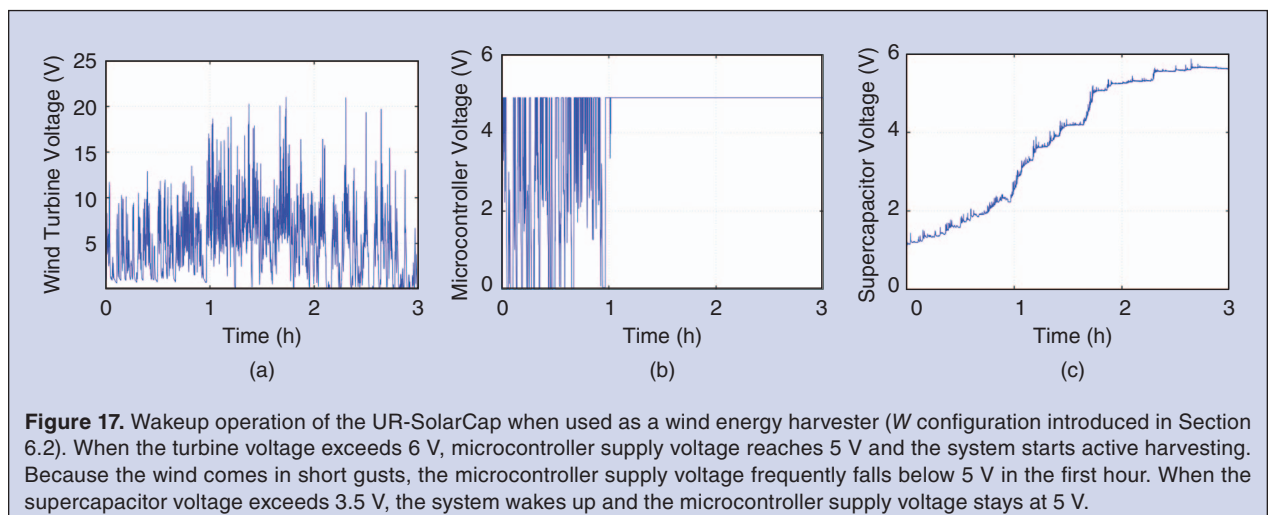
10.2. Wakeup Operation with a Wind Turbine

The original UR-SolarCap board [34] is a solar-only harvester that incorporates auto wake-up functionality, which allows it to resume normal operation from a fully depleted energy buffer state. In Section 6.2, we presented the necessary hardware and software modifications to

turn UR-SolarCap into a W harvester and confirmed its general harvesting functionality (Fig. 11). In this section, we provide experimental results validating the wake-up functionality of our W harvester. In this experiment, a fully-depleted 8×3000 F supercapacitor block was used as the energy buffer. The wind turbine voltage, microcontroller supply voltage, and the supercapacitor block voltage were logged. The results are shown in Fig. 17. When the supercapacitor voltage is less than 3.5 V and the input voltage is less than 6 V, the system is completely passive with the PIC microcontroller nonfunctional. As the input voltage rises above 6 V, wind power is supplied to the system through the wakeup path and the supercapacitor voltage starts increasing. Once the supercapacitor block exceeds 3.5 V, the system wakes up, the microcontroller becomes operational and starts intelligent harvesting, including MPPT. This can be seen in the figure as the constant 5 V supply voltage of the microcontroller in UR-SolarCap after the first hour.

10.3. Independent Solar/Wind Energy Harvesting

Figure 18 demonstrates the harvesting performance of the SW configuration (Section 7.1). This setup includes two UR-SolarCap boards, a solar panel, and a wind turbine. The instantaneous power of each source was measured through the measurement and communication module of UR-SolarCap [34]. Figure 18 clearly demonstrates the drastic differences between the nature of solar and wind power sources; while the power output of the solar panel exhibits gradual changes over time, the wind turbine supplies its power in short bursts peaking up to 30 W. The short power interruptions in Fig. 18, approximately every four minutes, are software induced by the fractional MPPT algorithm. The algorithm disconnects the solar panel from the harvester for these periods in order to measure the open-circuit voltage



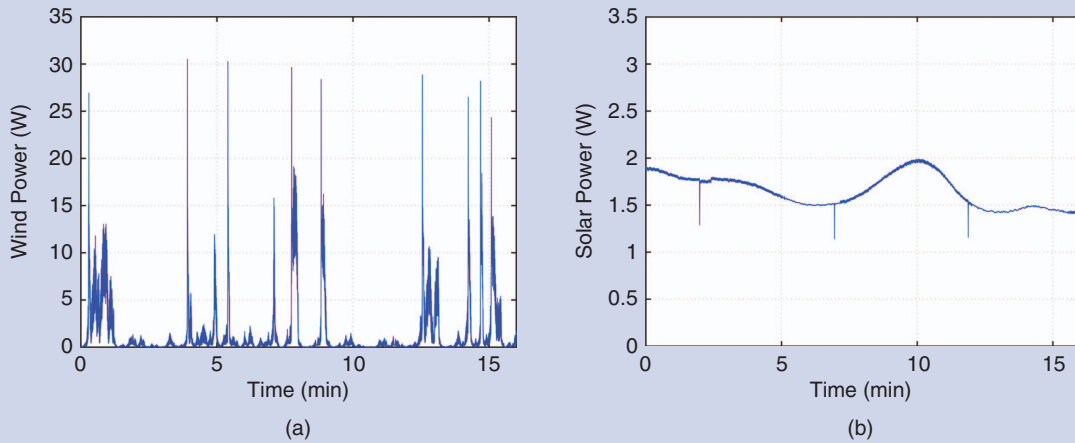


Figure 18. Input power from two UR-SolarCap harvesters in the S_W configuration over durations spanning 15 min. Although the wind power appears in short bursts (a), its average is approximately 1.2 W, which is comparable to the average solar power (right). The MPP is calculated approximately every four minutes in the solar harvester firmware, which is observed as the small interruptions in the solar power (b).

(V_{oc}) of the solar panel to set the (approximate) MPP operating point and no power is harvested over these short periods.

10.4. Cooperative Solar Energy Harvesting

The *Cooperative* mode discussed in Section 8 (and depicted in Fig. 13(c)) assigns the responsibility of setting the SEPIC duty cycle (for Board₁ and Board₂) to the master board (Board₁). An alternative approach that we tested allows both boards to perform their V_{oc} measurement and set their own duty cycle independently. However, this can cause an imbalance in their incom-

ing power, as depicted in Fig. 19, which plots the power inputs of Board₁ and Board₂ in the S_2S_2 configuration.

Our experimental setup to produce the results in Fig. 19 included two UR-SolarCap boards operating in *Cooperative* mode and two 2:1 analog MUXes, which connect two parallel 30 W solar panels to each of the harvesting boards. We do not present the results for cooperative multi-board harvesters in *Regular* mode, since their operation is identical to independent multi-board configurations in this mode.

Theoretically, since both boards are connected to the same power source, the calculated MPP is expected

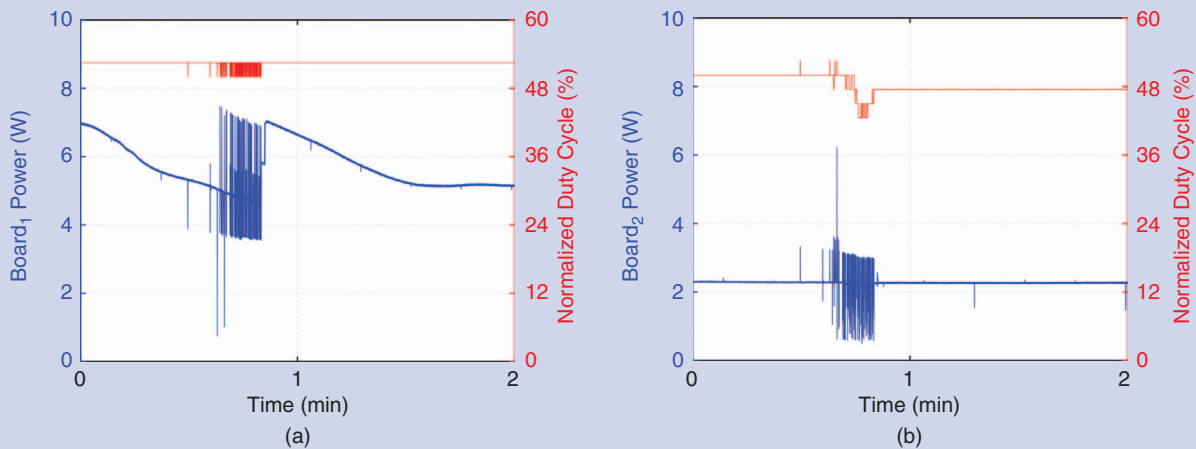


Figure 19. Experimental results for the S_2S_2 configuration, operating in *Cooperative* mode; one of the solar power sources was harvested by both boards cooperatively, while the other one was disconnected. During this experiment, Board₁ and Board₂ calculated their own SEPIC duty cycles independently, which ended up being slightly different; this led to an unbalanced power distribution, with Board₁ receiving 68% and Board₂ receiving 32% of the total available 8.35 W.

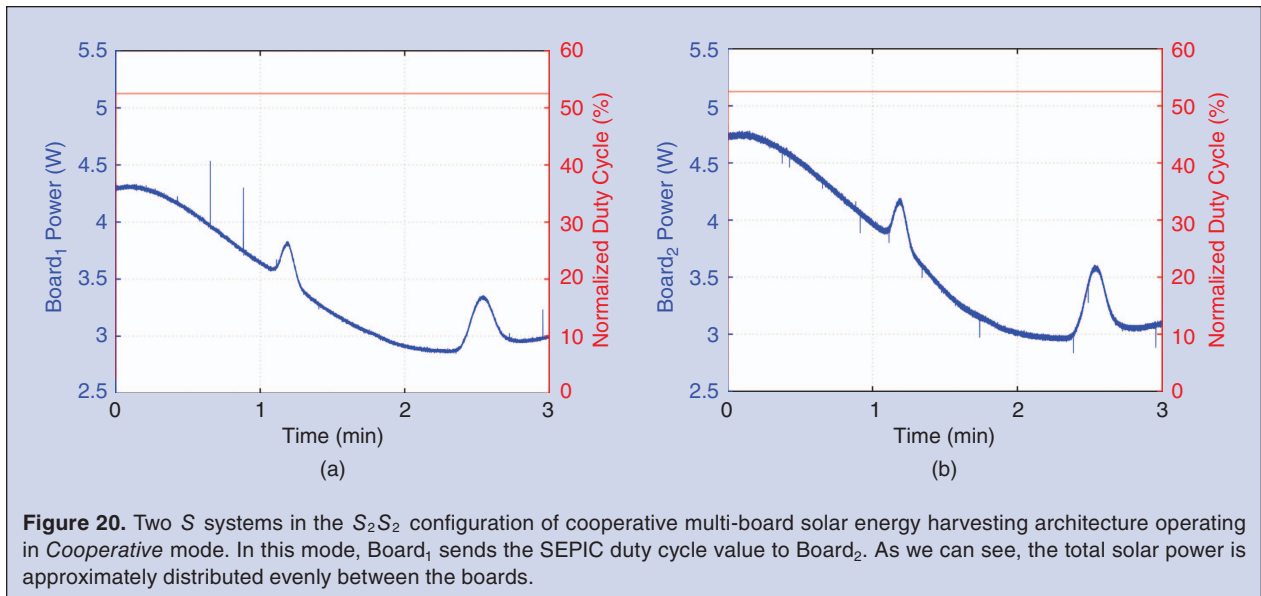


Figure 20. Two S systems in the S_2S_2 configuration of cooperative multi-board solar energy harvesting architecture operating in *Cooperative* mode. In this mode, Board₁ sends the SEPIC duty cycle value to Board₂. As we can see, the total solar power is approximately distributed evenly between the boards.

to be the same in both boards. However, due to the presence of noise in measurements, the determined SEPIC duty cycle values can be slightly different, leading to an unbalanced power distribution between the boards. The average power generated by the shared solar panel was approximately 8.35 W during the experiment. Board₁ received 5.65 W at its input, while Board₂ received 2.70 W on average, resulting in a load distribution of 68%–32%. At $t = 0.8$ minutes, both boards change their duty cycle value independently trying to keep the solar panel at their internally calculated V_{MPP} , causing the abrupt changes to the solar power input. Note that the generated solar power (8.35 W) is relatively low compared to the rated power of the solar panels (60 W), as the experiments were conducted during a cloudy day.

Figure 20 shows the operation of an S_2S_2 setup in *Cooperative* mode, in which the master board determines and shares the value of the SEPIC duty cycle. This implementation is based on our description of the cooperation mechanism in Section 8.2. As can be seen, the source power is evenly distributed between the master and slave boards, as they now use the same duty cycle value. During this experiment, the shared solar panel delivered ≈ 6.91 W on average, 3.55 W was distributed to Board₁ and 3.36 W to Board₂ corresponding to a 51% and 49% load split.

10.5. Cooperative Wind Energy Harvesting

Figure 21 depicts the operation of the cooperative multi-board configuration operating in *Cooperative* mode, where the master board calculates the SEPIC duty cycle and shares it with the slave. During this experiment, we connected a wind turbine to both of the

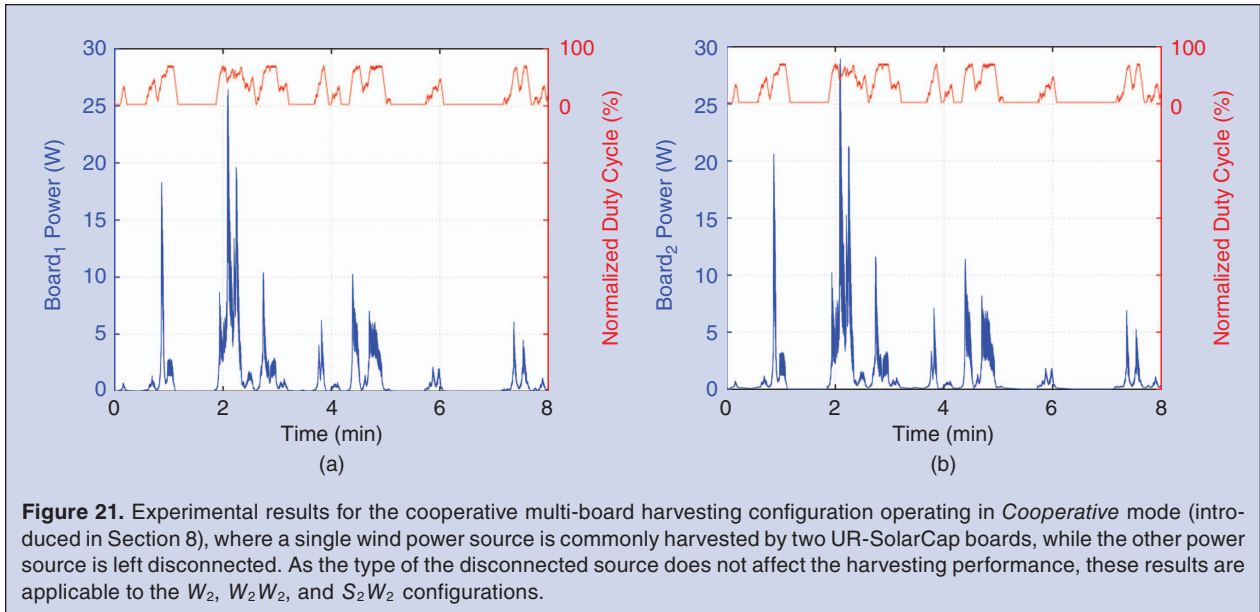
harvesting boards and programmed the firmware—of both boards—to stay in *Cooperative* mode, thereby jointly harvesting the single wind power source. The results of this experiment are applicable to the W_2W_2 , S_2W_2 , and W_2 harvesters, operating in *Cooperative* mode as follows:

- While both boards harvest a different wind power source independently in the *Regular* mode of a W_2W_2 harvester, they decide to switch to *Cooperative* mode when the power level of one of the sources increases substantially; in *Cooperative* mode, the wind turbine with higher power is harvested by both boards, through a configuration that is identical to our experimental setup;
- In S_2W_2 harvesters, solar and wind power sources are independently harvested by two boards in *Regular* mode, while the wind power source is harvested cooperatively when its power level increases significantly, prompting a switch to the *Cooperative* mode; this is exactly the experimental setup we have;
- The operation of a W_2 configuration is identical to our experimental setup already in *Cooperative* mode.

The results of this experiment are depicted in Fig. 21. During the experiment, Board₁ and Board₂ received an average power of 0.86 W and 0.88 W, respectively, which represents a load balance of 49% and 51%.

10.6. Time-multiplexed Energy Harvesting

To analyze the behavior of our time-multiplexed single-board architecture, we conducted an experiment on our $S \parallel S$ configuration (Section 10.6 and Fig. 14), in

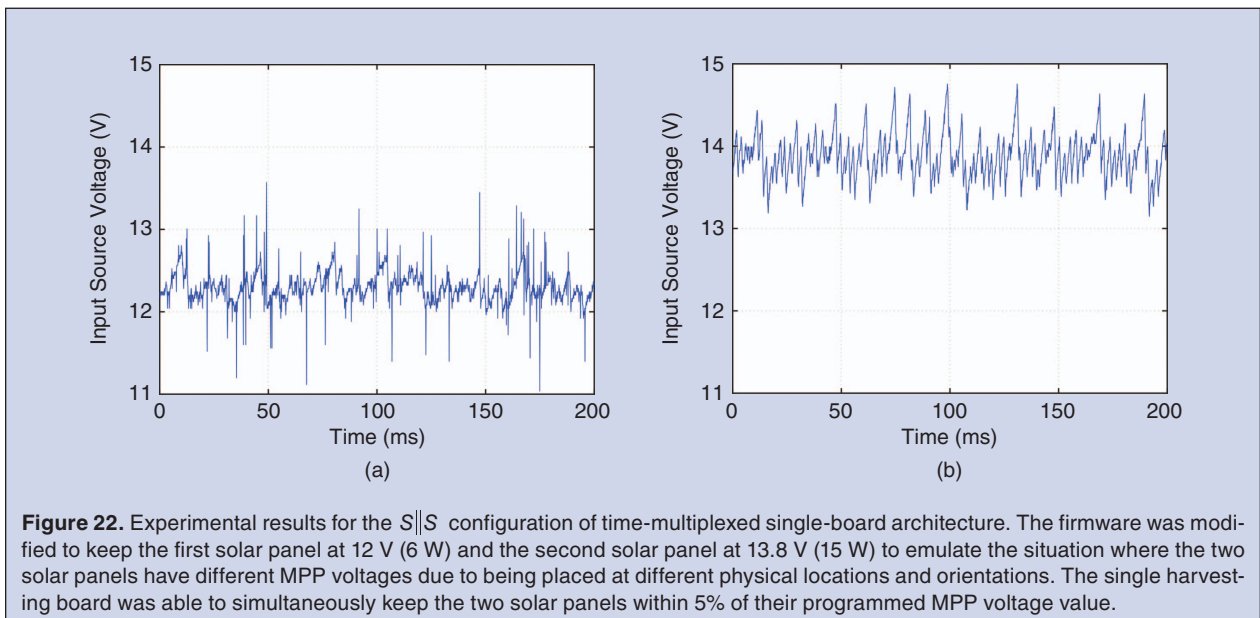


which two separate solar panels—with a rated power of 30 W—were connected to a single harvesting board through a 2:1 analog MUX. We programmed the harvesting board to keep the voltage of one solar panel at 12 V and the other at 13.8 V, thereby, simulating a situation where two panels are at different locations/orientations and have different V_{MPP} voltages. Considering the output power of solar panels (6 W and 15 W), we set the multiplexer round robin sequencing period to 3 ms and used a 100 μF input buffer capacitor for the UR-SolarCap board, which is connected to the *output* of the MUX. We used large 4700 μF capacitors at each *input* of the MUX for both power sources. This eliminates the situation

where each power source has a significant ripple during the switches.

Figure 22 depicts the results of our experiment. As discussed in Section 10.6, reducing the ripples around V_{MPP} is critical in time-multiplexed single board configurations to ensure high system efficiency (particularly due to η_{sw}). During this experiment, harvesting board was able to keep the panels' average voltage within $\pm 5\%$ of the programmed V_{MPP} values.

The total round-robin sequencing period of the MUX was 6 ms, during which each source was harvested for 3 ms. During the first 3 ms, the firmware adjusted the SEPIC duty cycle of the switching signal to D_1 , which



kept the first source at $V_{MPP1} = 12$ V; upon switching to the other source, the SEPIC duty cycle was instantly changed to D_2 to keep the second source at $V_{MPP2} = 13.8$ V during the second 3 ms interval. At the end of each 3 ms interval, the value of the SEPIC duty cycle was stored as the starting point for when the round-robin sequence selected this source again.

Which specialist should you see for diagnosing a spinal cord injury which specialist should you see for diagnosing a spinal cord injury

11. Conclusions and Future Work

In this paper, we reviewed solar and wind power harvesting, highlighted the utility of using these sources as a pair of complementary power sources, and presented several hybrid harvester architectures based on open-

source designs that combine solar/wind harvesting. Our analysis confirms that hybrid harvesters for solar/wind power sources allow embedded systems to be deployed with much less downtime, as compared to systems using solar or wind power alone. We provide four different classes of energy harvester system designs to cover a wide range of trade-offs between cost, complexity, fault-tolerance, and expandability. Table 10 lists the four categories of our designs, which are available as open-source designs from <http://www.ece.rochester.edu/projects/siplab/OpenWare/UR-SolarCap.html>, along with the designs for UR-SolarCap—the open-source solar-only harvester on which these designs are based.

Our first category is *single-source* harvesters, for which we introduce the notations S and W to denote *solar only* and *wind only*, respectively. While the S

Table 10.
A comparison among all presented configurations and their advantages/disadvantages, annotated using the symbols \uparrow and \downarrow , respectively. The choice of the best setting should be made according to the system’s applications and availability of power sources. Bullet points (\bullet) under the “Sources” column represent the number and type of the power sources in each configuration. For example, the $S \parallel S \parallel W$ configuration includes two solar panels and one wind turbine.

Architecture	Notation	Sources		Advantages/Disadvantages
		Solar	Wind	
Single-Source Single-Board	S	\bullet		\uparrow Simplicity
	W		\bullet	\downarrow Not Hybrid
Independent Multiple Board	SW	\bullet	\bullet	\uparrow Simplicity
	SS	$\bullet\bullet$		\uparrow Expandability
	WW		$\bullet\bullet$	\uparrow Fault-Tolerance
	SSS	$\bullet\bullet\bullet$		\downarrow Cost
	WWW		$\bullet\bullet\bullet$	
	SSW	$\bullet\bullet$	\bullet	
Cooperative Multiple Board	S_2	\bullet		\uparrow Increased P_{cell}
	W_2		\bullet	\uparrow Fault-Tolerance
	$S_2 S_2$	$\bullet\bullet$		\downarrow Simplicity
	$W_2 W_2$		$\bullet\bullet$	\downarrow Expandability
	$S_2 W_2$	\bullet	\bullet	\downarrow Cost
Time Multiplexed Single Board	$S \parallel S$	$\bullet\bullet$		\uparrow Cost
	$W \parallel W$		$\bullet\bullet$	\uparrow Expandability
	$S \parallel W$	\bullet	\bullet	\downarrow Fault-Tolerance
	$S \parallel S \parallel S$	$\bullet\bullet\bullet$		\downarrow Simplicity
	$W \parallel W \parallel W$		$\bullet\bullet\bullet$	
	$S \parallel W \parallel W$	\bullet	$\bullet\bullet$	
	$S \parallel S \parallel W$	$\bullet\bullet$	\bullet	

configuration is based on the original UR-SolarCap design, the W configuration is based on modified firmware for the UR-SolarCap board introduced in this paper.

In our second *independent multiple-board* hybrid harvester category, multiple UR-SolarCap boards harvest a single power source independently and buffer their output into the same supercapacitor block; we use the notations SW , SS , WW to denote hybrid power sources with two power inputs, *solar/wind*, *solar/solar*, and *wind/wind*, respectively. The SSS , WWW , SSW , and SWW notations denote three independent power sources, *solar/solar/solar*, \dots , *solar/wind/wind*. Despite its cost disadvantage, this category is highly expandable, because another power source can be very easily added by adding another UR-SolarCap board with its input connected to the new power source and its output to the common supercapacitor block. Furthermore, this category provides fault resilience against the malfunction of UR-SolarCap boards.

Our next hybrid harvester category is termed *cooperative multiple-board* and uses multiple UR-SolarCap boards. In contrast with the previous category, this new category allows multiplexing of different power sources into multiple UR-SolarCap boards. Such multiplexing introduces an advantage: if the power level of a specific power source is too high for a single UR-SolarCap board to handle at any given point in time (defined as P_{Ceil} in Eq. 25) and the power input of the other power source is fairly low, two UR-SolarCap boards can be used to harvest the same input, potentially doubling the harvested power. We introduce a subscript notation (\dots_2) to denote the number of UR-SolarCap boards, harvesting cooperatively; for example the S_2 and W_2 notations denote the configuration with two UR-SolarCap boards, with either a single solar (S_2) or a single wind (W_2) input, thereby permitting doubled harvesting capability for either power input. Similarly the S_2S_2 , W_2W_2 , and S_2W_2 notations denote two separate solar power inputs (S_2S_2), two separate wind power inputs (W_2W_2), and one wind and one solar power input (S_2W_2) being harvested cooperatively by two UR-SolarCap boards. Three power-input configurations of the cooperative harvesting, $S_3S_3W_3$, and $S_3W_3W_3$, denote the usage of three UR-SolarCap boards cooperatively harvesting *solar/solar/wind* and *solar/wind/wind* power inputs, the former being a good candidate for hybrid harvesting that uses two separate solar panels, facing the sun at two different angles to achieve a more steady solar power input throughout the day.

Our final hybrid harvester category is termed *time-multiplexed single-board*, which uses only a single UR-SolarCap board to harvest energy available at multiple power sources. This configuration uses time-multiplex-

ing to harvest each individual power source for only a portion of the time, while buffering the other power sources using small capacitors. This configuration has a cost advantage and lends itself well to expansion; however, it suffers from reduced fault tolerance, because the single UR-SolarCap board used in this configuration creates a single point of failure for all of the harvested power sources. We use the notations $S\|S$, $S\|W$, and $W\|W$ to denote a configuration that uses a single UR-SolarCap board, which time-multiplexes two power inputs, *solar/solar*, *solar/wind*, and *wind/wind*, respectively. The three-power-input versions of the same configuration are $S\|S\|S$, $W\|W\|W$, $S\|W\|W$ and $S\|S\|W$.

To test our designs, we conduct experiments on selected configurations of each architecture and evaluate their functionality. Our experimental results confirm the efficacy and versatility of our proposed system architectures and also highlight the advantages and disadvantages of each design, as listed in Table 10. In future work, we plan to introduce versions of our designs that are capable of harvesting a variety of other power sources, in addition to solar and wind.

Acknowledgment

This work was supported in part by the National Science Foundation grant CNS-1239423.



Mohamadhadi Habibzadeh received his B.S. in Computer Engineering from Isfahan University of Technology in Iran in 2015 and his M.S. degree in Technical Entrepreneurship and Management (TEM) from University of -Rochester, USA in 2016. He is currently pursuing his PhD degree in the Electrical and Computer Engineering department of University at Albany, State University of New York (SUNY Albany), under the supervision of Dr. Tolga Soyata. His current research interests include Cyber Physical systems and embedded systems with applications in Internet of Things and Smart Cities.



Moeen Hassanaliheragh received his B.S. degree in Electrical Engineering from Sharif University of Technology, Tehran, Iran in 2012. He joined the University of Rochester Electrical and Computer Engineering Department (UR ECE) in January 2014. He received his M.S. degree from UR ECE in 2015. He has been pursuing his PhD degree at UR ECE; until mid-2016, he was with Dr. Soyata's research group. His research interests includes energy aware computing, energy harvesting circuits, Cyber Physical Systems, and Terahertz Imaging.



Akihiro Ishikawa was an undergraduate student at the University of Rochester, ECE department until he received his BS ECE degree in 2016. He worked as an undergraduate research assistant, helping Dr. Sharma and Dr. Soyata with research in energy harvesting systems. He is currently pursuing his MS degree at Carnegie Mellon University.



Tolga Soyata (M'08 SM'16) received his B.S. degree in Electrical and Communications Engineering from Istanbul Technical University in 1988, M.S. degree in Electrical and Computer Engineering from Johns Hopkins University in 1992 and Ph.D. in Electrical and Computer Engineering from University of Rochester in 2000. He joined the University of Rochester ECE Department in 2008. He was an Assistant Professor—Research at UR ECE when he left to join SUNY Albany Department of ECE as an Associate Professor in 2016. His teaching interests include CMOS VLSI ASIC Design, FPGA-based High Performance Data Processing System Design, and GPU Architecture and Parallel Programming. His research interests include Cyber Physical Systems, Digital Health, and GPU-based high-performance computing. He is a senior member of both IEEE and ACM.



Gaurav Sharma (S'88-M'96-SM'00-F'13) is a professor at the University of Rochester in the Department of Electrical and Computer Engineering, in the Department of Computer Science and in the Department of Biostatistics and Computational Biology. He received the BE degree in Electronics and Communication Engineering from Indian Institute of Technology Roorkee (formerly Univ. of Roorkee), India in 1990; the ME degree in Electrical Communication Engineering from the Indian Institute of Science, Bangalore, India in 1992; and the MS degree in Applied Mathematics and PhD degree in Electrical and Computer Engineering from North Carolina State University, Raleigh in 1995 and 1996, respectively. From Aug. 1996 through Aug. 2003, he was with Xerox Research and Technology, in Webster, NY, initially as a Member of Research Staff and subsequently at the position of Principal Scientist. Dr. Sharma's research interests include data analytics, cyberphysical systems, signal and image processing, computer vision, media security, and communications. He is a fellow of the IEEE, of SPIE, and of the Society of Imaging Science and Technology (IS&T) and a member of Sigma Xi. From 2011 through 2015, he served as the Editor-in-Chief for the Journal of Electronic Imaging and in the past has served

as an associate editor for the Journal of Electronic Imaging, IEEE Transactions on Image Processing, and IEEE Transactions on Information Forensics and Security.

References

- [1] B. Morris and M. Trivedi, "Real-time video based highway traffic measurement and performance monitoring," in *Proc. IEEE Intelligent Transportation Systems Conf.*, Sept. 2007, pp. 59–64.
- [2] F. Qu, F. Y. Wang, and L. Yang, "Intelligent transportation spaces: Vehicles, traffic, communications, and beyond," *IEEE Commun. Mag.*, vol. 48, no. 11, pp. 136–142, Nov. 2010.
- [3] A. Zanella, N. Bui, A. Castellani, L. Vangelista, and M. Zorzi, "Internet of things for smart cities," *IEEE Internet Things J.*, vol. 1, no. 1, pp. 22–32, Feb. 2014.
- [4] M. Habibzadeh, Z. Qin, T. Soyata, and B. Kantarci, "Large scale distributed dedicated- and non-dedicated smart city sensing systems," *IEEE Sensors J.*, to be published.
- [5] V. Dyo, S. A. Ellwood, D. W. Macdonald, A. Markham, N. Trigoni, R. Wohlers, C. Mascolo, B. Pásztor, S. Scellato, and K. Yousef, "Wildsensing: Design and deployment of a sustainable sensor network for wildlife monitoring," *ACM Trans. Senors. Netw.*, vol. 8, no. 4, pp. 29:1–29:33, Sept. 2012.
- [6] F. Mehdipour, "Smart field monitoring: An application of cyber-physical systems in agriculture (work in progress)," in *Proc. IIAI 3rd Int. Conf. Advanced Applied Informatics*, Aug. 2014, pp. 181–184.
- [7] J. Burrell, T. Brooke, and R. Beckwith, "Vineyard computing: Sensor networks in agricultural production," *IEEE Pervasive Comput.*, vol. 3, no. 1, pp. 38–45, Jan. 2004.
- [8] J. McCulloch, P. McCarthy, S. M. Guru, W. Peng, D. Hugo, and A. Terhorst, "Wireless sensor network deployment for water use efficiency in irrigation," in *Proc. Workshop on Real-world Wireless Sensor Networks*, New York, 2008, pp. 46–50.
- [9] M. Habibzadeh, W. Xiong, M. Zheleva, E. K. Stern, B. H. Nussbaum, and T. Soyata, "Smart city sensing and communication sub-infrastructure," in *IEEE Midwest Symp. Circuits and Systems*, Boston, MA, Aug. 2017.
- [10] Q. Zhou, A. Sussman, J. Chang, J. Dong, A. Zettl, and W. Mickelson, "Fast response integrated MEMS microheaters for ultra low power gas detection," *Sensors Actuators A: Phys.*, vol. 223, pp. 67–75, 2015.
- [11] Y. Lee, S. Bang, I. Lee, Y. Kim, G. Kim, M. H. Ghaed, P. Pannuto, P. Dutta, D. Sylvester, and D. Blaauw, "A modular 1 mm³ die-stacked sensing platform with low power I²C inter-die communication and multi-modal energy harvesting," *IEEE J. Solid-State Circuits*, vol. 48, no. 1, pp. 229–243, Jan. 2013.
- [12] F. Dressler, S. Ripperger, M. Hierold, T. Nowak, C. Eibel, B. Cassens, F. Mayer, K. Meyer-Wegener, and A. Kolpin, "From radio telemetry to ultra-low-power sensor networks: Tracking bats in the wild," *IEEE Commun. Mag.*, vol. 54, no. 1, pp. 129–135, Jan. 2016.
- [13] M. H. Ghaed, G. Chen, R. u. Haque, M. Wieckowski, Y. Kim, G. Kim, Y. Lee, I. Lee, D. Fick, D. Kim, M. Seok, K. D. Wise, D. Blaauw, and D. Sylvester, "Circuits for a cubic-millimeter energy-autonomous wireless intraocular pressure monitor," *IEEE Trans. Circuits Syst. I*, vol. 60, no. 12, pp. 3152–3162, Dec. 2013.
- [14] S. Nawaz and C. Mascolo, "Mining users' significant driving routes with low-power sensors," in *Proc. 12th ACM Conf. Embedded Network Sensor Systems*, New York, 2014, pp. 236–250.
- [15] A. Dementyev and J. A. Paradiso, "Wristflex: Low-power gesture input with wrist-worn pressure sensors," in *Proc. 27th Annual ACM Symp. User Interface Software and Technology*, New York, 2014, pp. 161–166.
- [16] T. Torfs, T. Sterken, S. Brebels, J. Santana, R. van den Hoven, V. Spiering, N. Bertsch, D. Trapani, and D. Zonta, "Low power wireless sensor network for building monitoring," *IEEE Sensors J.*, vol. 13, no. 3, pp. 909–915, Mar. 2013.
- [17] A. Engel and A. Koch, "Heterogeneous wireless sensor nodes that target the internet of things," *IEEE Micro*, vol. 36, no. 6, pp. 8–15, Nov. 2016.
- [18] A. Somov, A. Baranov, D. Spirjakin, and R. Passerone, "Circuit design and power consumption analysis of wireless gas sensor nodes: One-sensor versus two-sensor approach," *IEEE Sensors J.*, vol. 14, no. 6, pp. 2056–2063, June 2014.
- [19] A. D. S. Bernabe, J. R. M. de Dios, and A. Ollero, "Efficient cluster-based tracking mechanisms for camera-based wireless sensor

- networks," *IEEE Trans. Mobile Comput.*, vol. 14, no. 9, pp. 1820–1832, Sept. 2015.
- [20] M. Imran, K. Shahzad, N. Ahmad, M. O'Nils, N. Lawal, and B. Oelmann, "Energy-efficient SRAM FPGA-based wireless vision sensor node: SENTIOF-CAM," *IEEE Trans. Circuits Syst. Video Technol.*, vol. 24, no. 12, pp. 2132–2143, Dec. 2014.
- [21] N. Kong and D. S. Ha, "Low-power design of a self-powered piezoelectric energy harvesting system with maximum power point tracking," *IEEE Trans. Power Electron.*, vol. 27, no. 5, pp. 2298–2308, May 2012.
- [22] Y. K. Ramadass and A. P. Chandrakasan, "A battery-less thermo-electric energy harvesting interface circuit with 35 mV startup voltage," *IEEE J. Solid-State Circuits*, vol. 46, no. 1, pp. 333–341, Jan. 2011.
- [23] A. Meehan, H. Gao, and Z. Lewandowski, "Energy harvesting with microbial fuel cell and power management system," *IEEE Trans. Power Electron.*, vol. 26, no. 1, pp. 176–181, Jan. 2011.
- [24] M. Piñuela, P. D. Mitcheson, and S. Lucyszyn, "Ambient RF energy harvesting in urban and semi-urban environments," *IEEE Trans. Microwave Theory Technol.*, vol. 61, no. 7, pp. 2715–2726, July 2013.
- [25] D. Ramasur and G. P. Hancke, "A wind energy harvester for low power wireless sensor networks," in *Proc. IEEE Int. Instrumentation and Measurement Technology Conf.*, May 2012, pp. 2623–2627.
- [26] C. Alippi and C. Galperti, "An adaptive system for optimal solar energy harvesting in wireless sensor network nodes," *IEEE Trans. Circuits Syst.*, vol. 55, no. 6, pp. 1742–1750, July 2008.
- [27] C. Park and P. H. Chou, "Power utility maximization for multiple-supply systems by a load-matching switch," in *Proc. Int. Symp. Low Power Electronics and Design*, Aug. 2004, pp. 168–173.
- [28] K. Y. Lo, Y. M. Chen, and Y. R. Chang, "MPPT battery charger for stand-alone wind power system," *IEEE Trans. Power Electron.*, vol. 26, no. 6, pp. 1631–1638, June 2011.
- [29] C. Liu, K. T. Chau, and X. Zhang, "An efficient wind photovoltaic hybrid generation system using doubly excited permanent-magnet brushless machine," *IEEE Trans. Ind. Electron.*, vol. 57, no. 3, pp. 831–839, Mar. 2010.
- [30] T. Soyata, L. Copeland, and W. Heinzelman, "RF energy harvesting for embedded systems: A survey of tradeoffs and methodology," *IEEE Circuits Syst. Mag.*, vol. 16, no. 1, pp. 22–57, Feb. 2016.
- [31] S. J. Roundy, "Energy scavenging for wireless sensor nodes with a focus on vibration to electricity conversion," Ph.D. dissertation, Univ. California, Berkeley, 2003.
- [32] S. Roundy, P. K. Wright, and J. Rabaey, "A study of low level vibrations as a power source for wireless sensor nodes," *Computer Commun.*, vol. 26, no. 11, pp. 1131–1144, 2003.
- [33] National Renewable Energy Laboratory. [Online]. Available: <http://rredc.nrel.gov/wind/pubs/atlas/tables/1-2T.html>
- [34] M. Hassanaliyagh, T. Soyata, A. Nadeau, and G. Sharma, "UR-Solar-Cap: An open source intelligent auto-wakeup solar energy harvesting system for supercapacitor based energy buffering," *IEEE Access*, vol. 4, pp. 542–557, Mar. 2016.
- [35] X. Lu and S.-H. Yang, "Thermal energy harvesting for WSNs," in *Proc. IEEE Int. Conf. Systems, Man and Cybernetics*, Oct. 2010, pp. 3045–3052.
- [36] R. Amiratharajah and A. P. Chandrakasan, "Self-powered signal processing using vibration-based power generation," *IEEE J. Solid-State Circuits*, vol. 33, no. 5, pp. 687–695, 1998.
- [37] S. D. Moss, O. R. Payne, G. A. Hart, and C. Ung, "Scaling and power density metrics of electromagnetic vibration energy harvesting devices," *Smart Mater. Struct.*, vol. 24, no. 2, pp. 023001, 2015.
- [38] X. Xing, J. Lou, G. Yang, O. Obi, C. Driscoll, and N. Sun, "Wideband vibration energy harvester with high permeability magnetic material," *Appl. Phys. Lett.*, vol. 95, no. 13, pp. 134103, 2009.
- [39] D. L. Churchill, M. J. Hamel, C. P. Townsend, and S. W. Arms, "Strain energy harvesting for wireless sensor networks," *Smart Struct. Mater.*, vol. 5055, pp. 319–327, 2003.
- [40] S. Boisseau, G. Despesse, and A. Sylvestre, "Optimization of an electret-based energy harvester," *Smart Mater. Struct.*, vol. 19, no. 7, pp. 075015, 2010.
- [41] A. Dewan, H. Beyenal, and Z. Lewandowski, "Scaling up microbial fuel cells," *Environ. Sci. Technol.*, vol. 42, no. 20, pp. 7643–7648, 2008.
- [42] B. R. Ringeisen, E. Henderson, P. K. Wu, J. Pietron, R. Ray, B. Little, J. C. Biffinger, and J. M. Jones-Meehan, "High power density from a miniature microbial fuel cell using shewanella oneidensis DSP10," *Environ. Sci. Technol.*, vol. 40, no. 8, pp. 2629–2634, 2006.
- [43] Y. K. Tan and S. K. Panda, "Energy harvesting from hybrid indoor ambient light and thermal energy sources for enhanced performance of wireless sensor nodes," *IEEE Trans. Ind. Electron.*, vol. 58, no. 9, pp. 4424–4435, 2011.
- [44] G. Honan, N. Gekakis, M. Hassanaliyagh, A. Nadeau, G. Sharma, and T. Soyata, "Energy harvesting and buffering for cyber physical systems: A review," in *Cyber Physical Systems: A Computational Perspective*. Boca Raton, FL: CRC, 2015, ch. 7, pp. 191–218.
- [45] K. M. Farinholt, G. Park, and C. R. Farrar, "RF energy transmission for a low-power wireless impedance sensor node," *IEEE Sensors J.*, vol. 9, no. 7, pp. 793–800, 2009.
- [46] B. Li, J. H. You, and Y.-J. Kim, "Low frequency acoustic energy harvesting using PZT piezoelectric plates in a straight tube resonator," *Smart Mater. Struct.*, vol. 22, no. 5, pp. 055013, 2013.
- [47] X. Jiang, J. Polastre, and D. Culler, "Perpetual environmentally powered sensor networks," in *Proc. Fourth Int. Symp. Information Processing in Sensor Networks*, Apr. 2005, pp. 463–468.
- [48] E. O. Torres and G. A. Rincon-Mora, "Electrostatic energy-harvesting and battery-charging CMOS system prototype," *IEEE Trans. Circuits Syst.*, vol. 56, no. 9, pp. 1938–1948, Sept. 2009.
- [49] M. Zhu, M. Hassanaliyagh, A. Fahad, Z. Chen, T. Soyata, and K. Shen, "Supercapacitor energy buffering for self-sustainable, continuous sensing systems," Dept. Computer Sci., Univ. Rochester, Tech. Rep. TR–995, Mar. 2016.
- [50] M. Hassanaliyagh, T. Soyata, A. Nadeau, and G. Sharma, "Solar-supercapacitor harvesting system design for energy-aware applications," in *Proc. 27th IEEE Int. System-on-Chip Conf.*, Las Vegas, NV, Sept. 2014, pp. 280–285.
- [51] A. Fahad, T. Soyata, T. Wang, G. Sharma, W. Heinzelman, and K. Shen, "SOLARCAP: Super capacitor buffering of solar energy for self-sustainable field systems," in *Proc. 25th IEEE Int. System-on-Chip Conf.*, Niagara Falls, NY, Sept. 2012, pp. 236–241.
- [52] A. Nadeau, G. Sharma, and T. Soyata, "State-of-charge estimation for supercapacitors: A kalman filtering formulation," in *Proc. IEEE Int. Conf. Acoustics, Speech and Signal Processing*, Florence, Italy, May 2014, pp. 2194–2198.
- [53] M. Habibzadeh, M. Hassanaliyagh, T. Soyata, and G. Sharma, "Supercapacitor-based embedded hybrid solar/wind harvesting system architectures," in *Proc. 30th IEEE Int. System-on-Chip Conf.*, Munich, Germany, Sept. 2017.
- [54] A. S. Weddell, M. Magno, G. V. Merrett, D. Brunelli, B. M. Al-Hashimi, and L. Benini, "A survey of multi-source energy harvesting systems," in *Proc. Design, Automation Test in Europe Conf.*, Mar. 2013, pp. 905–908.
- [55] D. Carli, D. Brunelli, L. Benini, and M. Ruggieri, "An effective multi-source energy harvester for low power applications," in *Proc. Design, Automation Test in Europe*, Mar. 2011, pp. 1–6.
- [56] C. Park and P. H. Chou, "AmbiMax: Autonomous energy harvesting platform for multi-supply wireless sensor nodes," in *Proc. 3rd Annu. IEEE Communications Society on Sensor and Ad Hoc Communications and Networks Conf.*, Sept. 2006, vol. 1, pp. 168–177.
- [57] M. Habibzadeh, M. Hassanaliyagh, T. Soyata, and G. Sharma, "Solar/wind hybrid energy harvesting for supercapacitor-based embedded systems," in *Proc. IEEE Midwest Symp. Circuits and Systems*, Boston, MA, Aug. 2017.
- [58] A. Du Pasquier, I. Plitz, S. Menocal, and G. Amatucci, "A comparative study of li-ion battery, supercapacitor and nonaqueous asymmetric hybrid devices for automotive applications," *J. Power Sources*, vol. 115, no. 1, pp. 171–178, 2003.
- [59] A. Nadeau, M. Hassanaliyagh, G. Sharma, and T. Soyata, "Energy awareness for supercapacitors using kalman filter state-of-charge tracking," *J. Power Sources*, vol. 296, pp. 383–391, Nov. 2015.
- [60] S. Wilcox. (2012, Aug.). National solar radiation database 1991–2010 update, National Renewable Energy Laboratory, US Department of Energy, Tech. Rep. [Online]. Available: http://rredc.nrel.gov/solar/old_data/nsrdb/1991-2010/
- [61] A. Hande, T. Polk, W. Walker, and D. Bhatia, "Indoor solar energy harvesting for sensor network router nodes," *Microprocessors Microsyst.*, vol. 31, no. 6, pp. 420–432, 2007.
- [62] A. Nasiri, S. A. Zabalawi, and G. Mandic, "Indoor power harvesting using photovoltaic cells for low-power applications," *IEEE Trans. Ind. Electron.*, vol. 56, no. 11, pp. 4502–4509, Nov. 2009.
- [63] J. A. Paradiso and T. Starner, "Energy scavenging for mobile and wireless electronics," *IEEE Pervasive Comput.*, vol. 4, no. 1, pp. 18–27, Jan. 2005.

- [64] B. Anspaugh, *GaAs Solar Cell Radiation Handbook*, 1996.
- [65] J. Britt and C. Ferekides, "Thin-film CdS/CdTe solar cell with 15.8% efficiency," *Appl. Phys. Lett.*, vol. 62, no. 22, pp. 2851–2852, 1993.
- [66] A. Rockett and R. Birkmire, "CuInSe₂ for photovoltaic applications," *J. Appl. Phys.*, vol. 70, no. 7, pp. R81–R97, 1991.
- [67] P. Würfel and U. Würfel, *Physics of Solar Cells: From Basic Principles to Advanced Concepts*. New York: Wiley, 2009.
- [68] G. Vachtsevanos and K. Kalaitzakis, "A hybrid photovoltaic simulator for utility interactive studies," *IEEE Trans. Energy Conversion*, vol. EC-2, no. 2, pp. 227–231, June 1987.
- [69] K. H. Hussein, I. Muta, T. Hoshino, and M. Osakada, "Maximum photovoltaic power tracking: An algorithm for rapidly changing atmospheric conditions," *IEEE Proc. Generation Transmission Distribut.*, vol. 142, no. 1, pp. 59–64, Jan. 1995.
- [70] T. Esmar and P. L. Chapman, "Comparison of photovoltaic array maximum power point tracking techniques," *IEEE Trans. Energy Conversion*, vol. 22, no. 2, pp. 439–449, June 2007.
- [71] J. J. Schoeman and J. D. V. Wyk, "A simplified maximal power controller for terrestrial photovoltaic panel arrays," in *Proc. IEEE Power Electronics Specialists Conf.*, June 1982, pp. 361–367.
- [72] W. Xiao and W. G. Dunford, "A modified adaptive hill climbing MPPT method for photovoltaic power systems," in *Proc. IEEE 35th Annu. Power Electronics Specialists Conf.*, June 2004, vol. 3, pp. 1957–1963.
- [73] C. Hua, J. Lin, and C. Shen, "Implementation of a DSP-controlled photovoltaic system with peak power tracking," *IEEE Trans. Ind. Electron.*, vol. 45, no. 1, pp. 99–107, Feb. 1998.
- [74] P. Midya, P. T. Krein, R. J. Turnbull, R. Reppa, and J. Kimball, "Dynamic maximum power point tracker for photovoltaic applications," in *Proc. 27th Annu. IEEE Power Electronics Specialists Conf.*, June 1996, vol. 2, pp. 1710–1716.
- [75] T. Khatib, A. Mohamed, N. Amin, and K. Sopian, "An efficient maximum power point tracking controller for photovoltaic systems using new boost converter design and improved control algorithm," *WSEAS Trans. Power Syst.*, vol. 5, no. 2, pp. 53–63, 2010.
- [76] E. Koutroulis and K. Kalaitzakis, "Design of a maximum power tracking system for wind-energy-conversion applications," *IEEE Trans. Ind. Electron.*, vol. 53, no. 2, pp. 486–494, Apr. 2006.
- [77] T. Thiringer and J. Linders, "Control by variable rotor speed of a fixed-pitch wind turbine operating in a wide speed range," *IEEE Trans. Energy Conversion*, vol. 8, no. 3, pp. 520–526, Sept. 1993.
- [78] S. M. Barakati, M. Kazerani, and X. Chen, "A new wind turbine generation system based on matrix converter," in *Proc. IEEE Power Engineering Society General Meeting*, June 2005, vol. 3, pp. 2083–2089.
- [79] W. Lu and B. T. Ooi, "Multiterminal LVDC system for optimal acquisition of power in wind-farm using induction generators," *IEEE Trans. Power Electron.*, vol. 17, no. 4, pp. 558–563, July 2002.
- [80] S. M. Barakati, M. Kazerani, and J. D. Aplevich, "Maximum power tracking control for a wind turbine system including a matrix converter," *IEEE Trans. Energy Conversion*, vol. 24, no. 3, pp. 705–713, Sept. 2009.
- [81] S. Chapman, *Electric Machinery Fundamentals*. Tata McGraw-Hill Education, 2005.
- [82] K. Amei, Y. Takayasu, T. Ohji, and M. Sakui, "A maximum power control of wind generator system using a permanent magnet synchronous generator and a boost chopper circuit," in *Proc. IEEE Power Conversion Conf.*, vol. 3, 2002, pp. 1447–1452.
- [83] National Oceanic and Atmospheric Administration. [Online]. Available: www.noaa.gov
- [84] P. Giorsetto and K. F. Utsurogi, "Development of a new procedure for reliability modeling of wind turbine generators," *IEEE Trans. Power Apparatus Syst.*, vol. PAS-102, no. 1, pp. 134–143, Jan. 1983.
- [85] S. H. Jangamshetti and V. G. Rau, "Normalized power curves as a tool for identification of optimum wind turbine generator parameters," *IEEE Trans. Energy Conversion*, vol. 16, no. 3, pp. 283–288, Sept. 2001.
- [86] S. Chalasani and J. M. Conrad, "A survey of energy harvesting sources for embedded systems," in *Proc. IEEE Southeast Conf.* Apr. 2008, pp. 442–447.
- [87] R. Morais, S. G. Matos, M. A. Fernandes, A. L. Valente, S. F. Soares, P. Ferreira, and M. Reis, "Sun, wind and water flow as energy supply for small stationary data acquisition platforms," *Computers Electron. Agri.*, vol. 64, no. 2, pp. 120–132, 2008.
- [88] M. Hassanaliyagh, A. Page, T. Soyata, G. Sharma, M. K. Aktas, G. Mateos, B. Kantarci, and S. Andreescu, "Health monitoring and management using internet-of-things (IoT) sensing with cloud-based processing: Opportunities and challenges," in *Proc. IEEE Int. Conf. Services Computing*, New York, June 2015, pp. 285–292.
- [89] A. Page, O. Kocabas, T. Soyata, M. K. Aktas, and J. Couderc, "Cloud-based privacy-preserving remote ECG monitoring and surveillance," *Ann. Noninvasive Electrocardiol.*, vol. 20, no. 4, pp. 328–337, 2014.
- [90] A. Page, S. Hijazi, D. Askan, B. Kantarci, and T. Soyata, "Research directions in cloud-based decision support systems for health monitoring using internet-of-things driven data acquisition," *Int. J. Services Comput.*, vol. 4, no. 4, pp. 18–34, 2016.
- [91] N. Gekakis, A. Nadeau, M. Hassanaliyagh, Y. Chen, Z. Liu, G. Honan, F. Erdem, G. Sharma, and T. Soyata, "Modeling of supercapacitors as an energy buffer for cyber-physical systems," in *Cyber Physical Systems: A Computational Perspective*. Boca Raton, FL: CRC, 2015, ch. 6, pp. 171–190.
- [92] D. Ravi, C. Wong, B. Lo, and G. Z. Yang, "A deep learning approach to on-node sensor data analytics for mobile or wearable devices," *IEEE J. Biomed. Health Inform.*, vol. 21, no. 1, pp. 56–64, Jan. 2017.
- [93] R. Pérez-Torres, C. Torres-Huitzil, and H. Galeana-Zapién, "Power management techniques in smartphone-based mobility sensing systems: A survey," *Pervasive Mobile Comput.*, vol. 31, pp. 1–21, 2016.
- [94] F. I. Simjee and P. H. Chou, "Efficient charging of supercapacitors for extended lifetime of wireless sensor nodes," *IEEE Trans. Power Electron.*, vol. 23, no. 3, pp. 1526–1536, May 2008.
- [95] Microchip PIC16F1789. [Online]. Available: <http://www.microchip.com/wwwproducts/en/PIC16F1783>
- [96] Designing DC/DC converters based on SEPIC topology, Texas Instruments [Online]. Available: <http://www.ti.com/lit/an/slyt309/slyt309.pdf>
- [97] O. Kocabas, T. Soyata, and M. K. Aktas, "Emerging security mechanisms for medical cyber physical systems," *IEEE/ACM Trans. Comput. Biol. Bioinform.*, vol. 13, no. 3, pp. 401–416, June 2016.
- [98] T. Soyata, *Enabling Real-Time Mobile Cloud Computing through Emerging Technologies*. IGI Global, 2015.
- [99] G. Honan, A. Page, O. Kocabas, T. Soyata, and B. Kantarci, "Internet-of-everything oriented implementation of secure digital health (D-Health) systems," in *Proc. IEEE Symp. Computers and Communications*, Messina, Italy, June 2016, pp. 718–725.
- [100] A. Page, M. Hassanaliyagh, T. Soyata, M. K. Aktas, B. Kantarci, and S. Andreescu, "Conceptualizing a real-time remote cardiac health monitoring system," in *Enabling Real-Time Mobile Cloud Computing through Emerging Technologies*, T. Soyata, Ed. IGI Global, 2015, ch. 1, pp. 1–34.
- [101] E. Koutroulis and K. Kalaitzakis, "Design of a maximum power tracking system for wind-energy-conversion applications," *IEEE Trans. Ind. Electron.*, vol. 53, no. 2, pp. 486–494, Apr. 2006.
- [102] S. M. R. Kazmi, H. Goto, H. J. Guo, and O. Ichinokura, "A novel algorithm for fast and efficient speed-sensorless maximum power point tracking in wind energy conversion systems," *IEEE Trans. Ind. Electron.*, vol. 58, no. 1, pp. 29–36, Jan. 2011.
- [103] Q. Wang and L. Chang, "An intelligent maximum power extraction algorithm for inverter-based variable speed wind turbine systems," *IEEE Trans. Power Electron.*, vol. 19, no. 5, pp. 1242–1249, Sept. 2004.
- [104] S. Morimoto, H. Nakayama, M. Sanada, and Y. Takeda, "Sensorless output maximization control for variable-speed wind generation system using IPMSG," *IEEE Trans. Ind. Applicat.*, vol. 41, no. 1, pp. 60–67, Jan. 2005.
- [105] E. Koutroulis, K. Kalaitzakis, and N. C. Voulgaris, "Development of a microcontroller-based, photovoltaic maximum power point tracking control system," *IEEE Trans. Power Electron.*, vol. 16, no. 1, pp. 46–54, Jan. 2001.
- [106] N. Femia, G. Petrone, G. Spagnuolo, and M. Vitelli, "Optimization of perturb and observe maximum power point tracking method," *IEEE Trans. Power Electron.*, vol. 20, no. 4, pp. 963–973, July 2005.
- [107] GNU Octave. [Online]. Available: <https://www.gnu.org/software/octave/about.html>
- [108] H. Mousazadeh, A. Keyhani, A. Javadi, H. Mobli, K. Abrinia, and A. Sharifi, "A review of principle and sun-tracking methods for maximizing solar systems output," *Renewable Sustain. Energy Rev.*, vol. 13, no. 8, pp. 1800–1818, 2009.